Brodogradnja Volume 76 Number 3 (2025) 76307

journal homepage: www.brodogradnja.fsb.hr

Brodogradnja

An International Journal of Naval Architecture and Ocean Engineering for Research and Development

CFD simulation of wave-induced motions of an LNG ship considering tank sloshing effects

Guangyan Jia[1], Jialong Jiao[1,], Chaohe Chen[1], Tiecheng Wu[2]*

[1] *School of Civil Engineering and Transportation, South China University of Technology, Guangzhou 510641, China*
[2] *School of Ocean Engineering and Technology, Sun Yat-sen University, Zhuhai 519000, China*

ARTICLE INFO

Keywords:
Liquefied natural gas carrier
Seakeeping
Tank sloshing
Internal and external flow coupling
Slamming pressure

ABSTRACT

This study uses a CFD approach to perform numerical simulations of the hydrodynamic interactions between LNG ship motions induced by waves and the sloshing behavior of cargo tanks. First, a CFD simulation is performed by solving the RANS equations to analyze the sloshing behavior of liquid in a three-dimensional rectangular tank subjected to forced simple harmonic motion. The accuracy of the RANS solver in addressing the sloshing problem is validated through comparisons with experimental data and other numerical methods. Next, the study considers the coupling effects of both the internal sloshing flow field and the external wave field on the motion of a simplified LNG vessel. The motion response of the LNG carrier in regular waves was simulated, and the sloshing impact pressure on the bulkheads under various conditions was analyzed. The simulation results of the LNG ship's hydrodynamic behavior were compared with experimental and numerical data from previous studies. The effect of liquid tank sloshing on ship motion and tank wall pressure was examined under both head and beam wave conditions. Additionally, different forward speeds under head wave conditions were considered. It is crucial to account for the coupled effects of tank sloshing and ship dynamics when designing and evaluating liquid cargo ships.

1. Introduction

With the ongoing advancement of the maritime industry and continuous improvements in shipbuilding technology, the construction of various types of liquid cargo vessels has increased considerably. This trend is especially apparent in the increasing number of very large crude carriers, liquefied natural gas carriers, and liquefied petroleum gas carriers. The increasing demand for energy fuel transportation, along with technological innovations in ship design and efficiency, has further accelerated the expansion of this sector [1]. As a result, greater attention is being paid to the safety of large liquid cargo vessels navigating through severe seas. When a ship's liquid tank is only partially filled, tank sloshing can greatly impact the hull's movement, particularly when the external wave frequency approaches the inherent frequency of the fluid in the container.

* Corresponding author.
E-mail address: jiaojl@scut.edu.cn

http://dx.doi.org/10.21278/brod76307
Received 28 January 2025; Received in revised form 14 May 2025; Accepted 24 May 2025
Available online 28 May 2025
ISSN 0007-215X; eISSN 1845-5859

Tank sloshing can generate violent impact loads, potentially leading to damage to the bulkhead structure. The considerable movement of the hull also, in turn, influences the tank sloshing loads [2]. Therefore, it is crucial to account for the coupled effect of tank sloshing and ship dynamics in the design and evaluation of liquid cargo vessels. Numerous studies have been performed on the issue of independent tank sloshing. For instance, Pistani and Thiagarajan [3] used experimental methods to measure the pressure generated by tank sloshing and proposed an effective solution for accurately monitoring bulkhead pressure during sloshing events. Godderidge et al. [4] used the modern modeling technique of response surface methodology to compare the numerical solution of tank sloshing pressure caused by the irregular translational and rotational motion of a ship, based on the wave spectrum, and contrasted these results with those obtained through Computational Fluid Dynamics (CFD) simulation. Antuono and Lugni [5] derived an analytical formula for the bulkhead pressure in rectangular tanks during tank sloshing and validated their findings using numerical calculation methods. Kaminski and Bogaert [6] analyzed the characteristics of sloshing pressure, cavitation, wave spray, and the elastic deformation resulting from tank sloshing.

Currently, there is limited research on the coupled simulation of internal and external flow fields in Liquefied Natural Gas (LNG) ships. Most related studies use potential flow theory to couple the vessel's motion with the tank flow sloshing problem. For instance, the dynamic behavior of an LNG vessel was analyzed using potential flow theory and compared with experimental results in Journée [7]. The findings confirm the method's effectiveness in accurately predicting the roll amplitude of an LNG ship with its tank at any loading rate. Molin [8] applied time-domain strip theory to solve the dynamics of liquid cargo ship responses under various wave conditions. Newman [9] used the WAMIT program to calculate the liquid sloshing behavior in the tanks of an LNG vessel under specific conditions in linear waves. This approach simultaneously solved the tank sloshing and ship motion in the time-domain, incorporating the sloshing load acting on the bulkhead into the ship motion equation. Kim et al. [10] solved the linear motion of an LNG ship using the impulse response function method, while the finite difference method was used to simulate the nonlinear tank sloshing. The results from both methods, for ship motion and tank sloshing, were then coupled. Tabri et al. [11] applied potential flow theory to investigate the sloshing interference problem of a liquid cargo ship when it moves toward another liquid cargo ship, validating their findings with tank model tests. Li et al. [12] studied the motion response of aquaculture ships and tank sloshing under rolling resonance, examining the interaction between ship movement and liquid dynamics in the tanks. Their study revealed that rolling resonance amplified liquid tank sloshing and negatively impacted ship stability. Martić et al. [13] explored the influence of liquid sloshing on ship motions and added resistance, using potential flow theory to model the interaction between ship dynamics and sloshing.

In recent years, with advancements in high-performance computation, the CFD method has become an effective tool for studying complex flow problems [14] and has been widely applied to investigate fluid dynamics issues in liquid cargo ships. Yue and Tang [15] studied three-dimensional large sloshing in both rectangular and cylindrical containers subjected to vertical and arbitrary excitations. Shen et al. [16] used the Reynolds Averaged Navier–Stokes (RANS) method to simulate the motion of a KVLCC2 with liquid tanks, comparing the effects of the presence and absence of liquid tanks on hull motion in head and beam wave scenarios. Yin et al. [17] used OpenFOAM to simulate the motion of a simplified LNG ship in head waves based on the RANS method and investigated the impact of tank sloshing on the ship's pitch and heave motions. Zhuang and Wan [18] used the naoe-FOAM-SJTU code to study sloshing dynamics in two prismatic tanks of an LNG carrier subjected to head waves. Jiao et al. [19] used the smooth particle hydrodynamics (SPH) method to examine the motion response of two LNG ships operating side by side in various wave conditions, comparing the results with those obtained using the CFD/RANS method. Wang et al. [20] indicated that the coupling effect was substantial around sloshing natural frequencies but tended to weaken under irregular wave actions. Liu et al. [21] used an unsteady RANS solver to investigate the influence of sloshing on a ship's parametric roll, focusing on the impact of liquid tank sloshing on the roll motion of LNG carriers. The results show that sloshing considerably reduces the roll decay rate of the ship model. In comparison to the model without liquid tanks, the presence of sloshing leads to a slower free roll decay process.

Additionally, the meshless SPH method has been applied to simulate the coupled responses of tank sloshing and ship motion. Ma and Oka [22] used the SPH method to illustrate the influence of strong nonlinearity in tank sloshing on ship motion and compared the results with those obtained using the linear boundary element method. Ding et al. [23] used the SPH method to simulate the coupled interactions between a floating barge and the sloshing flow in its tank. To investigate the effects of spatial dimensionality on these interactions, both two-dimensional and three-dimensional SPH simulations were performed. Cheng [24] developed an SPH simulation for single-phase flow, incorporating a free surface capture technique and a wave height calculation algorithm. This model effectively predicts both the pressure loads exerted on the bulkhead and the dynamic characteristics of the free surface. The SPH method, which incorporates a Riemann solver for particle interaction calculations, was used by Pilloton et al. [25], improving the stability and accuracy of pressure predictions during water impact events. Trimulyono et al. [26] investigated sloshing phenomena in prismatic tanks equipped with vertical and T-shaped baffles using the SPH method, exploring the effects of various baffle configurations on liquid motion and its interaction with the tank structure. This research contributes to a deeper understanding of sloshing dynamics in liquid transport systems.

The primary objective of this study is to provide a CFD-based tool for solving the problem of sloshing coupled with the seakeeping response of LNG ships. While previous research has explored the coupled responses of ship motions and tank sloshing through experiments and potential flow theory, investigations using CFD methods remain limited. Most previous CFD simulations have mainly focused on independent tank sloshing or ship seakeeping issues separately. In this study, numerical simulations of the seakeeping behavior of liquid cargo ships are performed using the CFD-based software STAR-CCM+. To validate the effectiveness of the RANS techniques applied in this study, independent tank sloshing is first simulated and compared with experimental results. Additionally, the motion of a liquid cargo ship is simulated under the coupled effects of internal and external flow fields. The motions of the LNG carrier, along with tank sloshing, are analyzed and compared under varying loading rates, wave frequencies, and ship speeds.

2. Basic theory

The theory presented in this section focuses on solving the problem of independent tank sloshing and the seakeeping of LNG ships under the coupling of internal and external flow fields. The numerical calculations are performed using the CFD/RANS-based software STAR-CCM+. The Finite Volume Method (FVM) implemented in STAR-CCM+ discretizes the integral form of the Navier–Stokes equations over control volumes, ensuring the conservation of mass, momentum, and energy. A second-order upwind scheme is used for spatial discretization, while temporal integration is performed using a second-order implicit unsteady solver. The pressure-velocity coupling is managed using the Semi-Implicit Method for Pressure Linked Equations (SIMPLE) algorithm [27]. By solving the conservation equations for mass, momentum, and energy of the fluid, the integral form of the incompressible RANS equation is solved using the FVM. To capture the free surface and the interface between fluids, the Volume of Fluid (VOF) method is used, which tracks the volume fraction of each fluid in a computational cell. The interface reconstruction and advection are handled using the High-Resolution Interface-Capturing scheme [28]. The motion of the rigid-body was simulated using the Dynamic Fluid Body Interaction (DFBI) module in STAR-CCM+, which solves the six degrees-of-freedom equations for bodies interacting with the fluid domain [29]. The k–ω SST turbulence model was used, combining the wall-adjacent robustness of the k–ω model with the free-stream independence of the k–ε model in the far field. This model is commonly used for external flow simulations, particularly those involving separation and vortex shedding [30].

In Cartesian coordinates, the continuity equation for a three-dimensional, unsteady, incompressible fluid is given by:

$$\frac{\partial \rho}{\partial t} + \nabla \cdot (\rho \mathbf{v}) = 0 \tag{1}$$

where ρ represents the density of the fluid, $\mathbf{v}$ is the velocity vector, which can be decomposed into (u, v, w) in space; t is the time variable, and ∇ is the Hamiltonian operator.

The momentum equation is given by:

$$\frac{\partial \mathbf{v}}{\partial t}+(\mathbf{v}\cdot\nabla)\mathbf{v}=-\frac{1}{\rho}\nabla p+\nu\nabla^{2}\mathbf{v}+f \tag{2}$$

where **v** is the velocity vector of the fluid, ρ is the density of the fluid, and f represents external forces acting on the fluid.

$$\begin{cases}\gamma=0,\ \text{air}\\ 0<\gamma<1,\ \text{interface}\\ \gamma=1,\ \text{water}\end{cases} \tag{3}$$

where γ represents the volume fraction of each component. When $\gamma = 0$, the fluid in the cell is air; when $\gamma = 1$, the fluid is water; and when $0 < \gamma < 1$, the fluid is a mixture of water and air. The fluid density and dynamic viscosity in the cell can then be described as follows:

$$\rho=(1-\gamma)\rho_{\text{air}}+\gamma\rho_{\text{water}} \tag{4}$$

$$\mu=(1-\gamma)\mu_{\text{air}}+\gamma\mu_{\text{water}} \tag{5}$$

In the formula, the subscripts "air" and "water" denote the density or viscosity of air and water, respectively, in the computational domain.

In the numerical calculation of turbulent flow, the relationship between viscosity and velocity of the turbulent vortex, as described by Boussinesq, is derived using the Realizable *k-omega* turbulence model. The turbulent kinetic energy k and the turbulent energy dissipation rate ε, as provided by the Realizable *k-omega* model, are governed by the following two transport equations:

$$\frac{\partial k}{\partial t}+U_{j}\frac{\partial k}{\partial x_{j}}=P_{k}-\beta^{*}k\omega+\frac{\partial}{\partial x_{j}}\left(\left(\mu+\mu_{t}\right)\frac{\partial k}{\partial x_{j}}\right) \tag{6}$$

where k is the turbulent kinetic energy, P_k is the generation term for turbulent kinetic energy, β^* is a constant related to the dissipation rate, μ is the dynamic viscosity, and μ_t is the turbulent dynamic viscosity. ω represents the turbulent dissipation rate. An implicit solver, based on the SIMPLE algorithm, is used to solve the pressure-velocity coupling equation.

The incident wave is modeled using the fifth-order Stokes wave, accounting for its nonlinear effects. The wave profile is described using the following equation:

$$\eta=\frac{1}{k}\sum_{n=1}^{5}\eta_{n}\cos\left[n\left(kx-\omega t\right)\right] \tag{7}$$

where η is the wave surface elevation, ω is the wave frequency, and k is the wave number.

The wave forcing method is used to enforce specified wave shapes near the boundary regions. This is accomplished by adding a source term to the transport equations in the form:

$$q_{\varphi}=\gamma\rho\left(\varphi-\varphi^{*}\right) \tag{8}$$

where γ is the forcing coefficient, ρ is the fluid density, φ is the current solution of the transport equation, and φ^{*} is the value toward which the solution is forced. The wave forcing method forces the Navier–Stokes equations toward a solution based on a simplified theory. This method preserves the wave form more effectively than the traditional wave-damping method.

3. Verification and validation of numerical simulation for liquid tank sloshing

In this section, the slam pressure on the inner bulkheads of a rectangular liquid tank is simulated using STAR-CCM+, with a comparison made to the numerical simulation results of Kang and Lee [31] and experimental data for validation. As shown in Figure 1(a), a three-dimensional model of the rectangular liquid tank is created. The tank's dimensions are: length L = 0.8 m, width W = 0.35 m, and height H = 0.5 m. The hydrostatic water level in the tank is set at h = 0.15 m. Horizontal excitation is applied to induce simple harmonic motion, with linear displacement along the length direction of the tank.

$$x = A\sin(\omega t) \tag{9}$$

where the amplitude A = 0.02 m and the circular frequency ω = 4.967 rad/s.

In the CFD/RANS solver, a specific domain is defined to represent the interface between water and air, with the VOF method used to accurately capture the boundary between these two phases. The governing equation is based on the *k-omega* turbulence model, with $y+$ set to 1. Additionally, the viscous bottom layer is solved directly during the computation. To monitor the sloshing pressure on the bulkhead, a pressure monitoring point P0 is set at a height of 0.115 m from the bottom on the left side of the bulkhead.

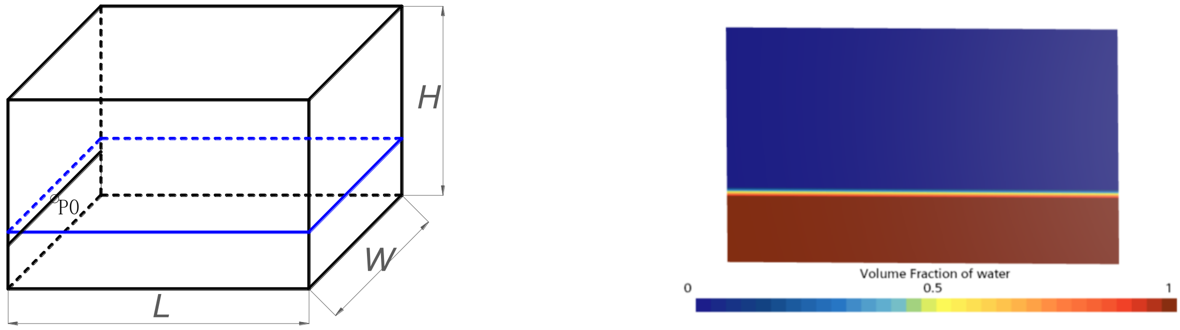

(a) 3D tank model **(b)** Numerical model

Fig. 1 Tank model and filling condition

3.1 Convergence analysis

A convergence analysis is crucial to assess the accuracy of mesh size and time step in numerical simulations. Three grid schemes were selected based on the fundamental grid size: 0.02 m (fine grid, 173,000 cells), 0.05 m (medium grid, 100,000 cells), and 0.1 m (coarse grid, 51,000 cells). The grid dimension in the vertical direction is set to 0.25 times the basic grid size to better capture the free surface during tank sloshing. The three grid configurations are shown in Figure 2. Additionally, time steps of t = 0.002 s (small), t = 0.003 s (medium), and t = 0.004 s (large) were chosen for the time step convergence analysis.

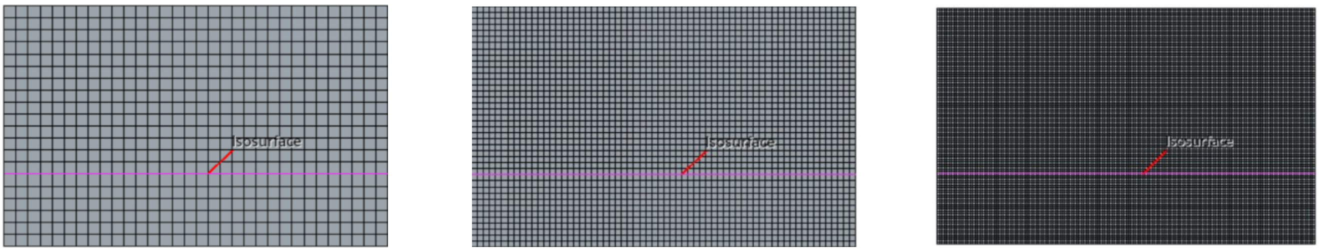

(a) Coarse grid **(b)** Medium grid **(c)** Fine grid

Fig. 2 Different meshes of the tank

Figure 3 shows a comparison of the sloshing pressures monitored at P0, calculated using three different grid sizes and time steps. As seen in Figure 3(a), the pressure peaks from the fine and medium grids are in close agreement, while the pressure peaks from the coarse grid are generally smaller and exhibit a phase lag. In Figure 3(b), the pressure time history curves obtained with time steps of 0.002 and 0.003 s are nearly identical. However, when the time step is increased to 0.004 s, a noticeable decay in the peak pressure occurs.

Based on these results, a time step of 0.003 s and a grid size of 0.05 m are selected for the subsequent calculations.

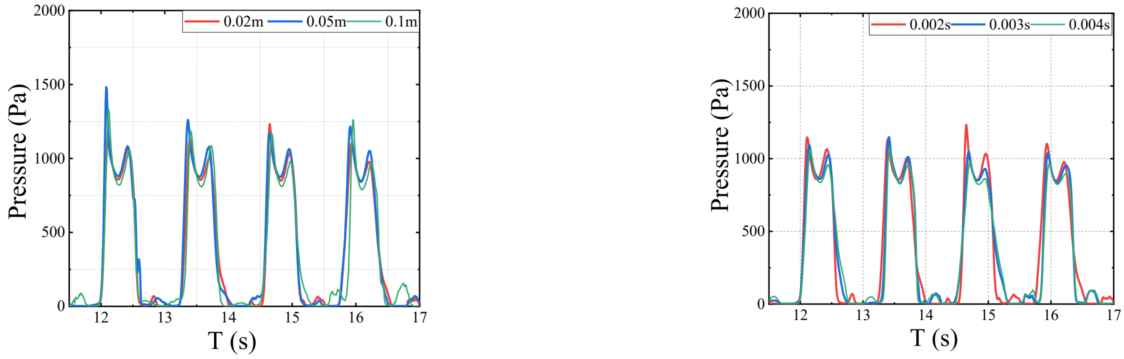

(a) Grid size analysis **(b)** Time step analysis

Fig. 3 Convergence analysis of tank sloshing

3.2 Accuracy validation

The time history curve of the slam pressure at P0 on the side bulkheads of the rectangular liquid tank is shown in Figure 4, comparing the present RANS simulation results with the experimental data provided by Xie et al. [32]. The peak value and impact period between the numerical results and the experimental data are in good agreement. An evident double peak phenomenon is observed at the pressure peak, which occurs because the wave group generated by the liquid tank sloshing creates a reflected wave upon reaching the bulkhead. The reflected wave then combines with the traveling wave generated by the sloshing, leading to this double peak effect.

In addition, a non-viscous model of the fluid domain was also used for calculation. This was achieved by disabling the viscous terms in the governing equations, specifically by choosing the inviscid option in the physics model section. This setup ensures that the simulation disregards viscous shear stresses, making it suitable for scenarios where viscosity effects are negligible. Additionally, for compressible flows, ensure that the turbulence model is set to off to maintain a purely inviscid flow condition. A comparison of the simulated pressure results between the RANS (viscous) model, the non-viscous model and the experimental data is shown in Figure 4. As depicted, both the RANS and inviscid simulations exhibit pressure fluctuation patterns that closely follow the experimental measurements, with only minor discrepancies observed in peak values.

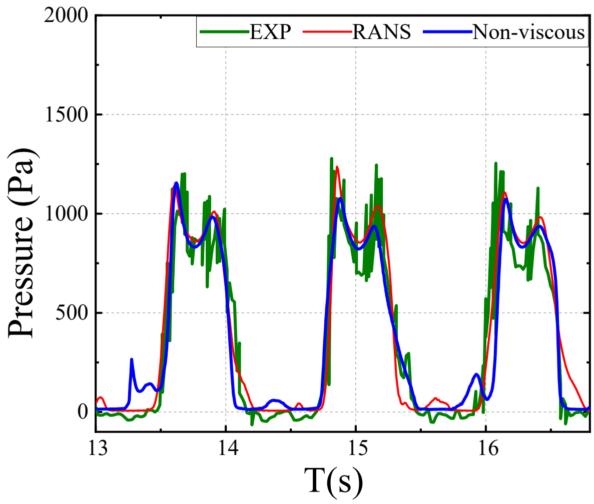

Fig. 4 Comparison of sloshing pressure between the numerical simulation and the experiment

Figure 5 shows the distribution of the free surface in the liquid tank at two characteristic time instants, t = 14.86 s and t = 15.18 s, comparing the RANS method, MPS simulation, and the experimental results from Xie et al. [32]. It is evident that the sloshing flow and free liquid levels obtained from the RANS simulation align well with both the experimental data and the MPS method, confirming the accuracy of the present RANS algorithm. While the RANS simulation captures the overall trend of the impact pressure and is consistent with the experimental observations, it has limitations in accurately modeling the liquid splash phenomenon. This can be attributed to the inherent constraints of mesh-based methods in tracking complex free-surface flows, whereas meshless particle methods, such as MPS, are better equipped to capture nonlinear splash and wave-breaking dynamics.

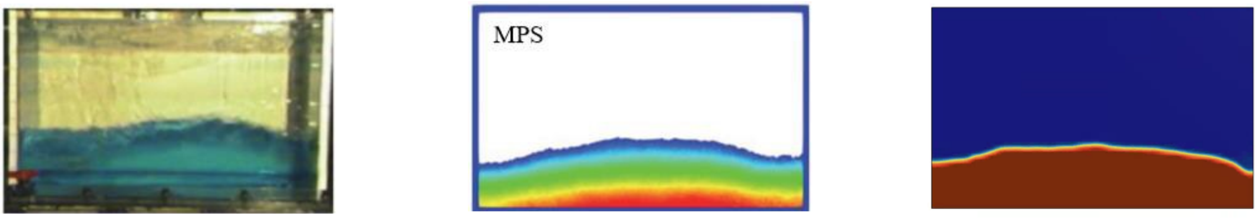

Experiment MPS RANS

(a) t = 14.86 s

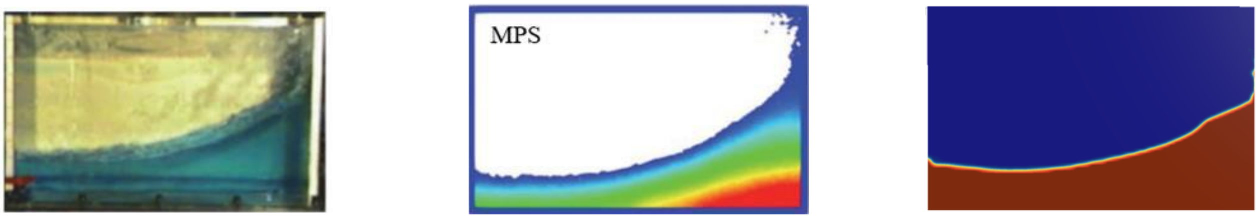

Experiment MPS RANS

(b) t = 15.18 s

Fig. 5 Tank sloshing at typical time instants

4. LNG ship and numerical tank setup

4.1 Description of the LNG ship

In this section, a simplified LNG vessel model is used to numerically simulate the seakeeping behavior of a liquid cargo ship in waves. The LNG hull contains two prismatic tanks. The three-dimensional geometry of the simplified LNG hull and the liquid cargo tank is shown in Figure 6. The numerical model is constructed at a scale ratio of 1/100. The main dimensions of the ship model and the tank model are provided in Tables 1 and 2, respectively. Additional details regarding the parameters of the LNG ship and tanks can be found in Jiao et al. [19].

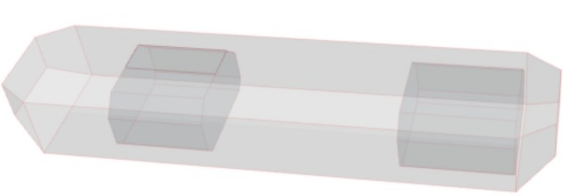

(a) Simplified LNG ship

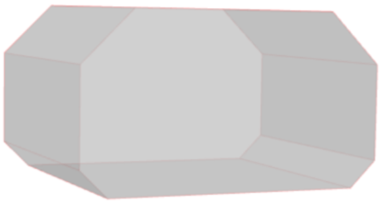

(b) Liquid cargo tank

Fig. 6 Geometry of the LNG ship and tank

Table 1 Main parameters of the LNG ship

Parameters	Value
Length overall L/m	2.85
Molded breadth B/m	0.63
Draft T/m	0.13
Displacement Δ/kg	220
Longitudinal center of gravity (from midship 10 station) xg/m	0
Vertical center of gravity (from baseline) zg/m	0.13
Roll radius of inertia Kxx/m	0.1945
Pitch radius of inertia Kyy/m	0.7125

Table 2 Main parameters of the liquid tank

Parameters	Bow tank	Stern tank
Length l/m	0.4696	0.5660
Width b/m	0.4692	0.4692
Height h/m	0.3223	0.3223

The natural frequency of sloshing flow in a rectangular liquid tank can be estimated using the following equation:

$$\omega_n = \sqrt{\frac{n\pi g}{L_{\text{tank}}}\tanh\left(\frac{n\pi h}{L_{\text{tank}}}\right)} \tag{10}$$

where ω_n is the nth-order natural frequency, g is the gravitational acceleration, L_{tank} is the characteristic length of the tank sloshing, and h is the filling height of the water. Table 3 presents the 1st-order natural frequency of tank sloshing for each condition.

Table 3 Summary of the 1st-order natural frequency of tank sloshing

Loading rate	Tank	Beam wave		Head wave	
		ω_1 (rad/s)	ω_1 $(L/g)^{1/2}$	ω_1 (rad/s)	$\omega_1(L/g)^{1/2}$
20 %	Bow tank	5.166	2.784	5.162	2.782
	Stern tank	5.166	2.784	4.321	2.329
57.5 %	Bow tank	7.450	4.016	7.446	4.013
	Stern tank	7.450	4.016	6.487	3.496
70 %	Bow tank	7.716	4.159	7.712	4.157
	Stern tank	7.716	4.159	6.796	3.663

4.2 Numerical model setup

As shown in Figure 7, a rectangular fluid domain with dimensions $-2L < x < 2L$, $0 < y < 1.5L$, and $-1.5L < z < 1.5L$ is defined in the STAR-CCM+ solver. The origin of the fluid domain's coordinate system is placed at the intersection of the hull's central longitudinal plane, the midship cross-section, and the still water surface. The overset mesh technique is used to simulate the large amplitude motion of the hull in waves. In the overlap region between the overset and background mesh areas, there are at least five mesh layers, with linear interpolation used to couple the overset mesh with the background region. A hexahedral unstructured mesh is used to generate the grid in the computational domain. To accurately capture the rapid variations in physical quantities, such as the free surface and turbulence around the hull, local mesh refinement is applied around the free surface and the hull, as shown in Figure 8. The grid size around the free surface is determined based on the wave height and wavelength of the incident waves.

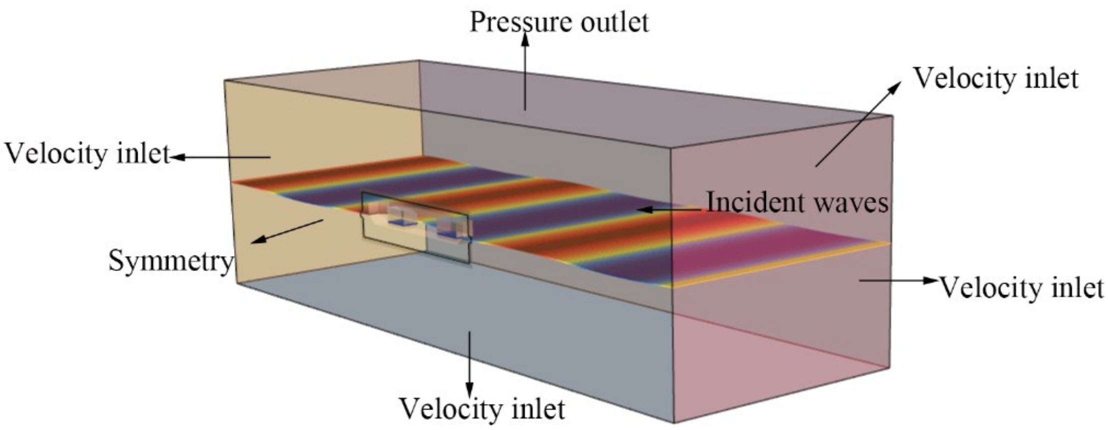

Fig. 7 Flow field computational domain and boundary conditions

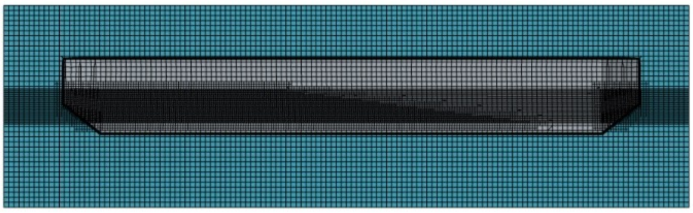

(a) Overset grid

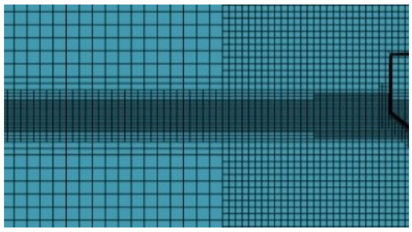

(b) Local grid refinement

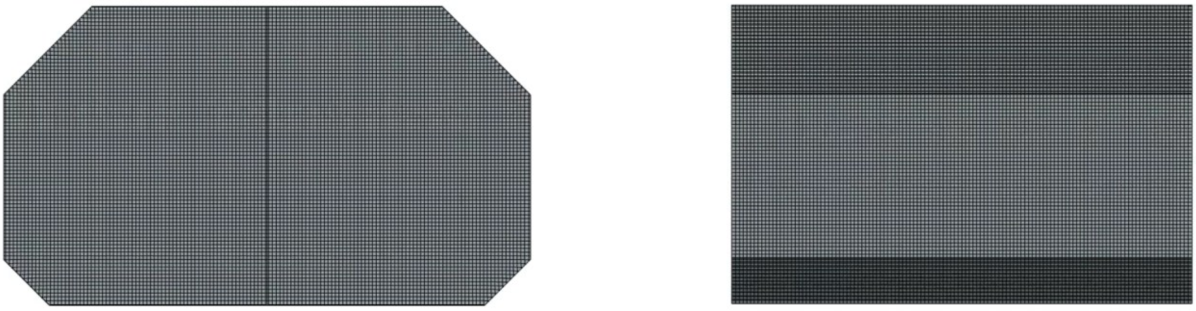

(c) Grid on the liquid tank

Fig. 8 Flow field computational domain and mesh generation

As shown in Figure 9, the wave forcing method is used to generate regular waves by forcing the wave pattern in the fluid domain as desired. To prevent wave reflection at the boundaries, the reflected waves are absorbed in a boundary zone located 1.2L away from both ends. To simulate the sloshing behavior of the internal tank inside the ship, it is necessary to define a field function that determines the spatial position of the liquid in the tank. This is achieved by developing a scalar function in the field function, which is set as the initial value according to the tank's initial conditions. The DFBI framework is used to model the simultaneous movement of the liquid tank and the ship hull. This framework enables the simulation of a freely floating vessel subjected to both external wave forces and internal sloshing loads, allowing for six degrees-of-freedom motion responses. The computational domain is divided into two regions: the external water domain, where regular incident waves interact with the ship hull, and the internal tank domain, where liquid motion is resolved using the VOF method to capture the free surface deformation of the sloshing fluid. The ship geometry is incorporated in an overset mesh configuration. This allows the ship to move freely in a stationary background grid. The DFBI module calculates the resultant hydrodynamic forces and moments acting on the hull by integrating the pressure and viscous stresses from both the external flow field and the internal fluid. The coupling calculation is performed during the time-marching process. The external wave field and internal tank sloshing generate pressure distributions on the hull surface, which are integrated to update the ship's translational and rotational motion via the rigid-body solver. The updated position and orientation of the hull are then used to recalculate the relative motion of the internal fluid, completing the coupling loop. The motion equations of the ship are solved simultaneously with the Navier-Stokes equations. A schematic view of the initialized internal and external flow fields is shown in Figure 10.

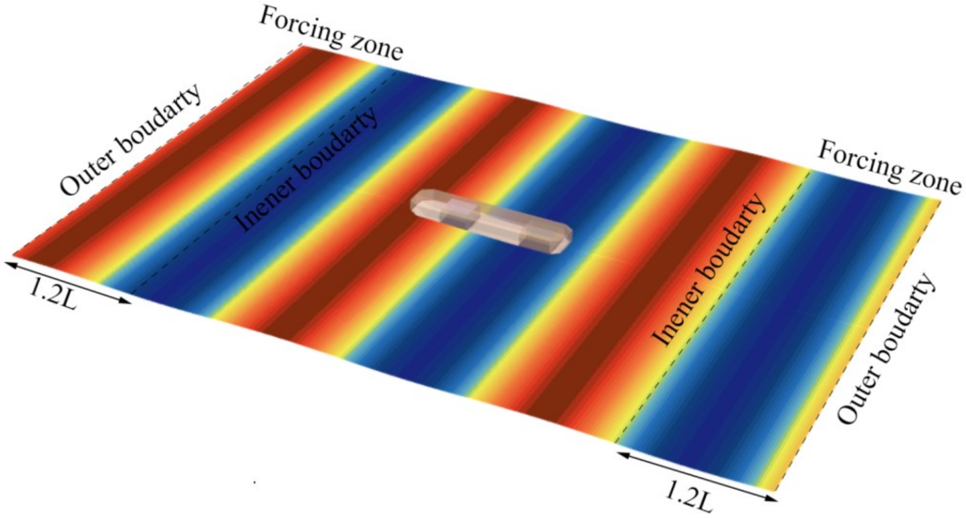

Fig. 9 Definition of the wave forcing zones and the boundaries

(a) External flow field and waves **(b)** Internal flow field in the tank

Fig. 10 Internal and external flow fields of the LNG carrier

In the seakeeping calculations, three degrees-of-freedom for ship motion - heave, roll, and pitch - are allowed to move freely, while the remaining three degrees-of-freedom are restricted. The typical conditions used in this study are summarized in Table 4. Incident wave angles of 180° and 90° correspond to head waves and beam waves, respectively. For all tank loading conditions (0 %, 20 %, 57.5 %, 70 %), the total mass of the ship and its moment of inertia are kept constant. To achieve this, the ship's weight and the position of its center of gravity are adjusted according to the varying filling rates, as outlined in Table 5. The reference origin point is located at the intersection of the baseline and the aft perpendicular.

The numerical simulation ensures that the draft of the LNG ship remains consistent across different loading rates, and that the ship's mass for each loading rate equals the sum of the mass of the liquids stored in the tanks and the ship's lightweight. Consequently, the total mass of the LNG ship for all loading rates is adjusted to a constant value of 220 kg. The center of mass and moment of inertia of the LNG tankers vary with different loading rates. Detailed information is provided in Table 5.

Table 4 Simulation conditions for LNG ship seakeeping behavior

Case	Wave direction	Wave parameters		Ship speed, Fr	Tank loading rate
		Frequency, $\omega(L/g)^{1/2}$	Amplitude, ζa/mm		
1−6	180°	1.0, 2.0, 2.5, 3.0, 3.25, 4.0	25	0	20 %
7	90°	2.0	25	0	20 %
8	180°	3.25	50	0	20 %
9−12	180°	2.0	50	0	0, 20 %, 57.5 %, 70 %
13−16	90°	2.0	50	0	0, 20 %, 57.5 %, 70 %
17−19	180°	2.0	25	0.1, 0.2, 0.3	20 %

Table 5 Basic information for the LNG ship at different loading rates

Tank loading rate	Center of gravity (x, y, z) (m)	Moment of inertia (Ixx, Iyy) (kg·m^2)	Ship light weight (kg)
0%	(1.425, 0, 0.3)	(8.640, 111.684)	220
20 %	(1.461, 0, 0.034)	(7.422, 95.936)	189
57.5 %	(1.527, 0, 0.092)	(5.184, 67.003)	132
70 %	(1.685, 0, 0.127)	(4.439, 56.340)	111

The computational work was performed on the High-Performance Computing Platform at South China University of Technology, which is equipped with Intel Xeon 6458Q and Hygon 7,380 processors, along with a 200 Gb/s InfiniBand network. Simulations were performed using STAR-CCM+ v2406, using 32 cores per case, with an average CPU time of approximately 36 h. Storage and data management were handled by a ParaStor300S system with a 34.45 PB capacity.

4.3 Free roll decay behavior

To investigate the roll motion behavior of the ship, including its natural period and damping ratio, simulations of free roll decay were performed both with and without different tank filling rates. The results of the roll decay curves for various filling rates are shown in Figure 11. Table 6 provides a summary of the natural period and damping ratio for each case. From the results, it can be observed that the free roll decay period is 1.31 s for the 0 % filling rate case, while it increases to 2.12 s under the 20 % liquid loading rate condition. At filling rates of 57.5 % and 70 %, the roll-free decay periods are 1.51 and 1.58 s, respectively, which are nearly identical. This indicates that the tank filling rate has a substantial impact on the roll-free decay period, suggesting that the tank sloshing phenomenon can change the ship's natural roll frequency.

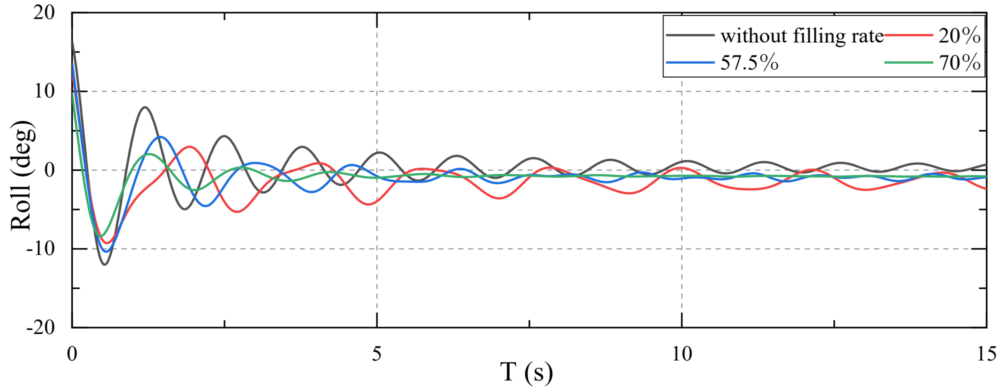

Fig. 11 Free decaying roll of the LNG carrier at different filling rates

Table 6 Roll decay period and frequency at different tank filling rates

Filling rate	Roll decay period (s)	Damping ratio
0%	1.31	0.19
20%	2.12	0.50
57.5%	1.51	0.41
70%	1.58	0.37

5. Motion response of the LNG ship in regular waves

5.1 Comparison of theoretical and numerical simulation waves

Before performing the seakeeping simulation of the ship, waves are generated in the numerical tank without the vessel present. Case 2 is selected for wave simulation using CFD/RANS. The wave parameters are $\omega(L/g)^{1/2} = 2.0$, $T = 1.69$ s, and $\zeta_a = 25$ mm. Figure 12 shows the wave elevation of the theoretical fifth-order Stokes wave compared with the waves generated by the numerical simulations. The results demonstrate that regular fifth-order Stokes waves can be accurately simulated using STAR-CCM+, which is essential for the subsequent study of the hydrodynamic behavior of liquid cargo vessels.

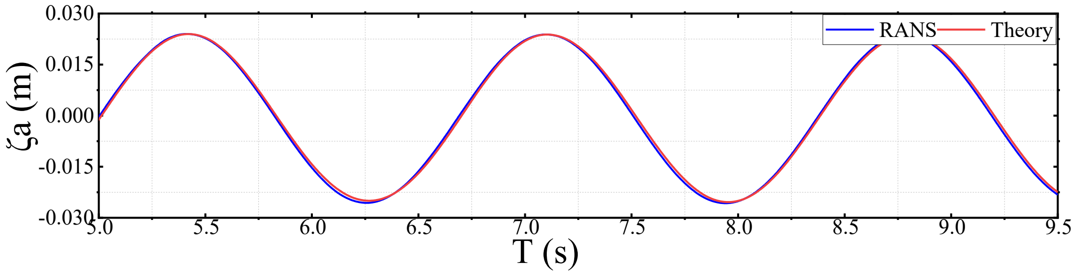

Fig. 12 Comparison of wave elevation between numerical simulation and theoretical data

5.2 Validation of the motion response of the LNG ship

The coupled dynamics of the simple LNG carrier's motion and the sloshing behavior of the liquid (water) inside the cargo tank are simulated. To investigate the vessel's response to regular waves, typical Case 2 is selected. This simulation provides an in-depth analysis of how the incident waves influence both the ship's motion and the sloshing behavior of the liquid in the tank. Time series of ship heave and pitch motions are shown in Figure 13. The RANS results are also compared with those obtained using the SPH method in Jiao et al. [19], where the open-source code DualSPHysics is used to solve the same LNG carrier's motions and tank sloshing in regular waves. The results demonstrate that the RANS method yields reliable ship motion predictions in regular waves. In this typical condition, the tank sloshing amplitude is small, meaning the impact of tank sloshing on the ship's motion response and slamming pressure is minimal. Figure 14 shows the movement of the LNG ship at four key time instants in one wave period, comparing the RANS simulation results with the SPH results from Jiao et al. [19]. The figure shows strong agreement between the RANS and SPH methods, especially in capturing the motion dynamics and internal sloshing behavior in the LNG vessel. The results from both methods validate their reliability in simulating the complex dynamics of the LNG ship system. In this case, the computational time for the SPH method is approximately 72 h, whereas the CFD method requires approximately 36 h.

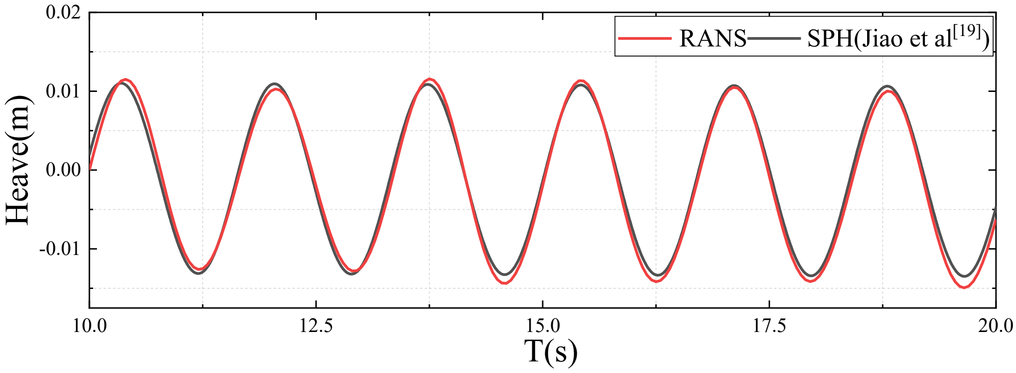

(a) Heave

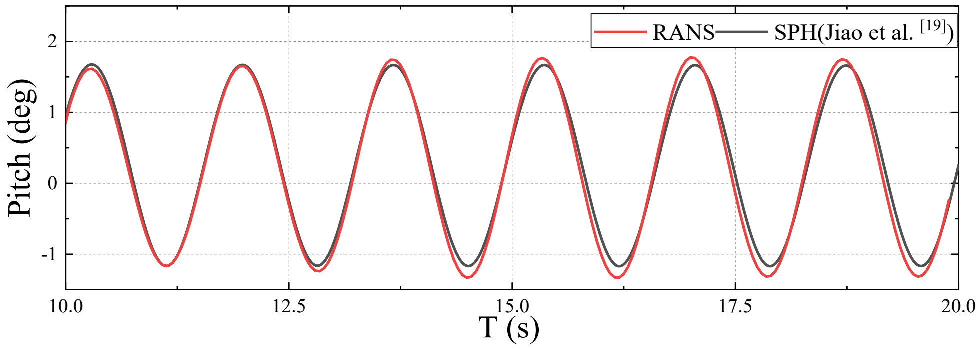

(b) Pitch

Fig. 13 Comparison of the time history of the ship's longitudinal motions in head waves (Case 2)

In references, Gou et al. [33] used the Rankine panel method based on time-domain potential flow theory to determine the motions of a ship with liquid sloshing phenomena for the same LNG vessel. Nam et al. [34] performed experiments with the same LNG vessel in the rectangular towing tank at Seoul National University. The results from Cases 1–6 are used to plot the response amplitude operators (RAOs). Heave and pitch motion RAOs are shown in Figure 15, providing a detailed comparison between the current RANS numerical simulation and the reference results from SPH simulations in Jiao et al. [19], the potential flow theoretical results in Gou et al. [33], and the experiment results in Nam et al. [34]. The comparison of RAOs obtained from different methods generally shows strong consistency, further validating the accuracy of the current RANS approach in simulating the responses of liquid cargo ships under regular waves.

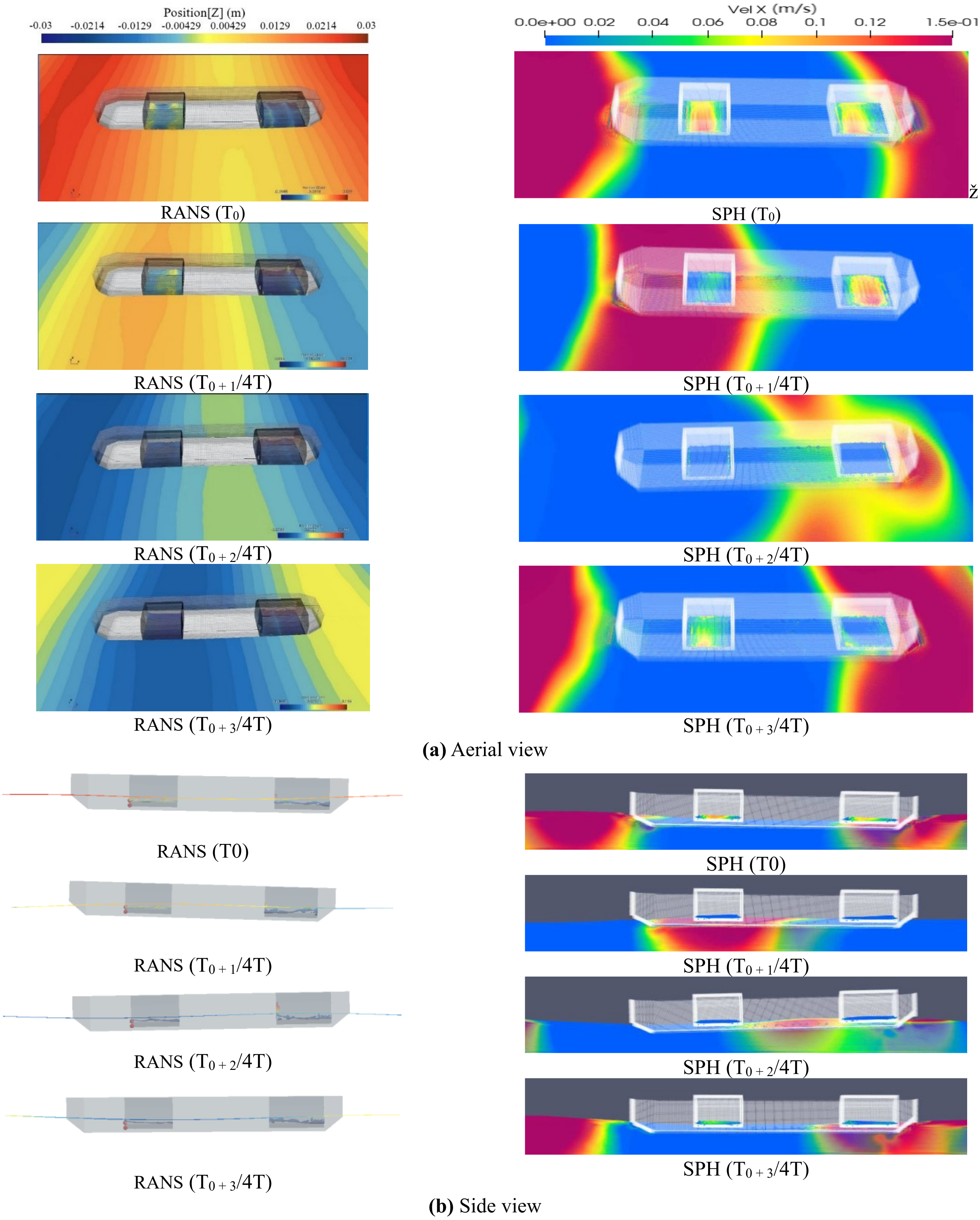

Fig. 14 Comparison of inside and outside flow fields at typical time instants between RANS and SPH (Case 2)

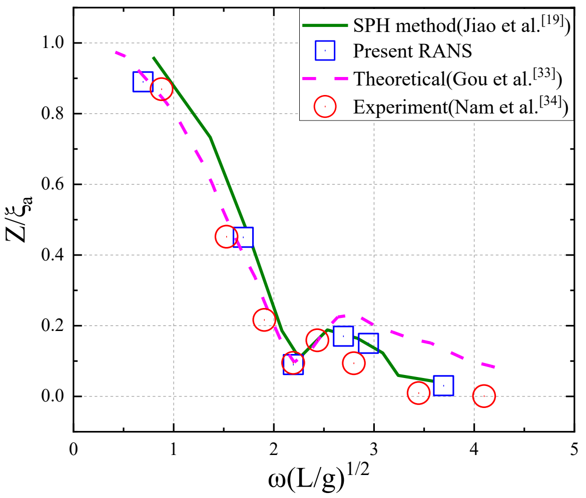

(a) Heave

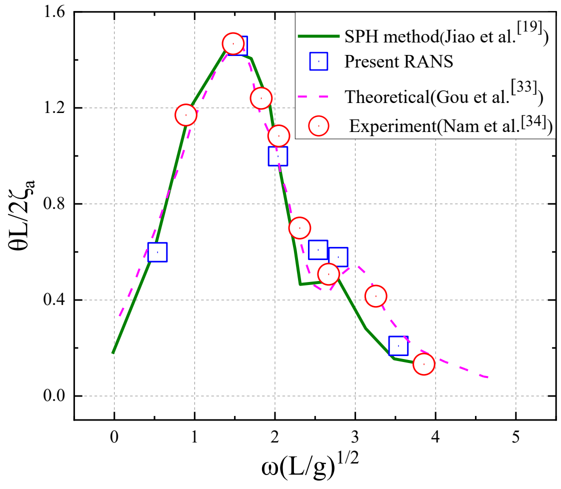

(b) Pitch

Fig. 15 Comparison of ship motion RAO in head waves using different methods (Cases 1–6)

5.3 Effect of tank loading rate on ship motion under head waves

In this section, the motion response of the LNG ship at various loading rates (0 %, 20 %, 57.5 %, and 70 %) under head waves (Cases 9–12) is presented and analyzed. For these cases, the wave frequency $\omega(L/g)^{1/2}$ = 2.0 and wave amplitude ζa = 50 mm are used. Figure 16 compares the time history curves of the ship's heave and pitch motion responses under different loading conditions. The amplitude of the heave motion for the LNG ship in head waves shows minimal variation at the 0 %, 20 %, and 57.5 % loading rates, but the heave amplitude increases by 38 % when the loading rate increases to 70 %. On the other hand, as the loading rate increases, the pitch amplitude gradually increases. Figure 17 shows the motion of the ship at a 20 % filling rate under head waves for Case 10. Figure 18 shows a comparison of the internal and external fluid field distributions around the LNG ship in head waves at different loading rates when the ship is in hogging condition.

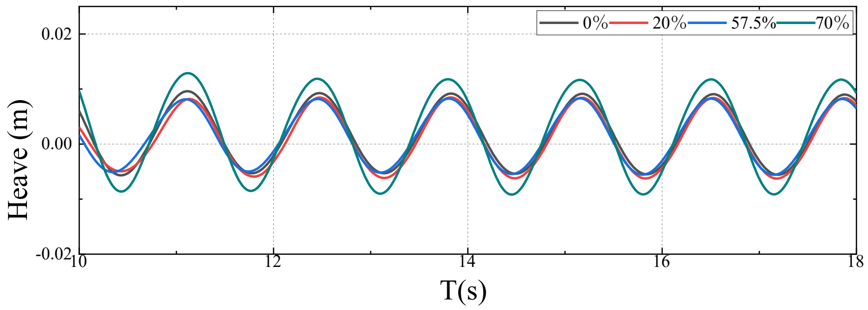

(a) Heave

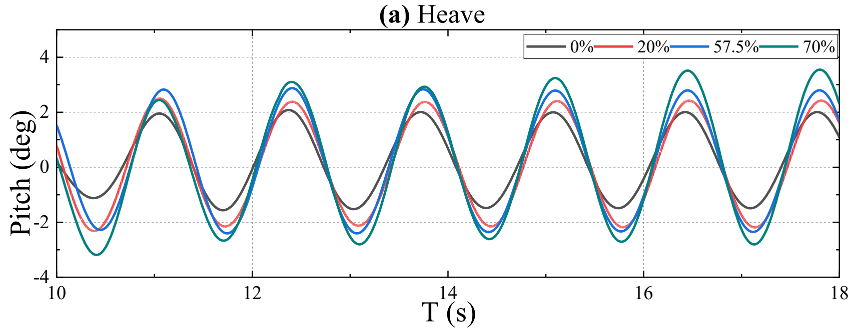

(b) Pitch

Fig. 16 Time history curve of ship motions in head waves at different loading rates (Cases 9–12)

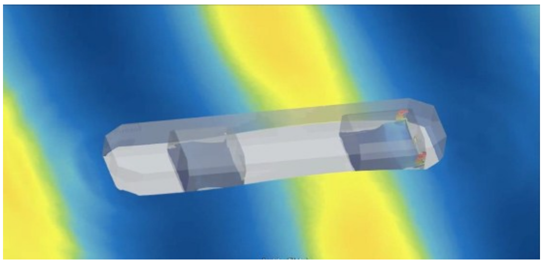

t = T0

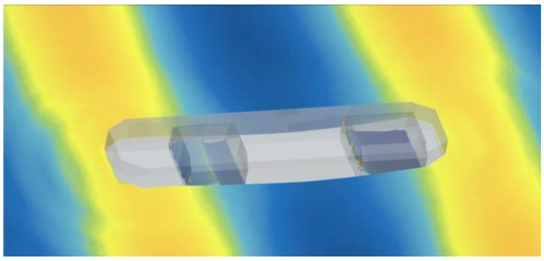

t = T0 + 1/4T

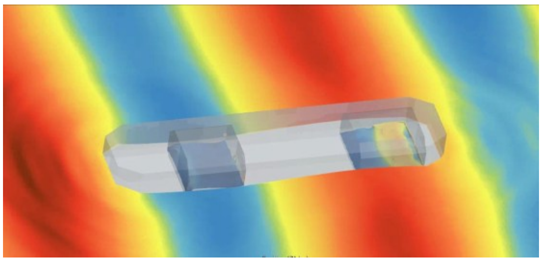

t = T0 + 2/4T

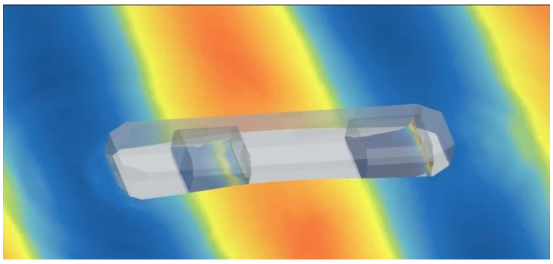

t = T0 + 3/4T

Fig. 17 Motion procedure of the ship at 20 % filling rate in head waves (Case 10)

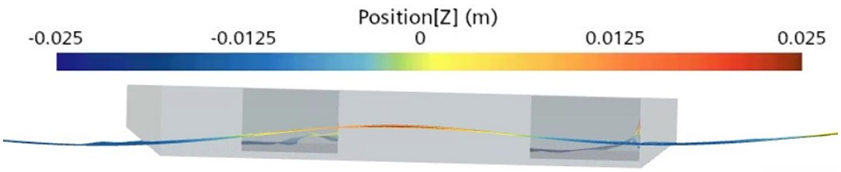

(a) 20 % filling rate

(b) 57.5 % filling rate

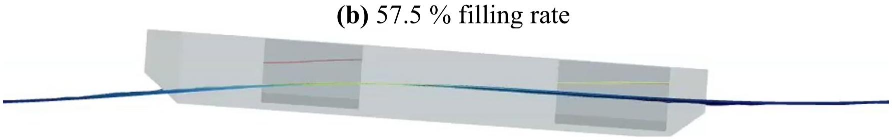

(c) 70 % filling rate

Fig. 18 Inner and external fluid field distribution of the ship at different loading rates in head waves (Cases 10–12)

5.4 Influence of tank loading rate on ship motions in beam waves

In this section, the motion of the LNG ship at various loading rates (0 %, 20 %, 57.5 %, and 70 %) under beam wave conditions (Cases 13–16) is presented and analyzed. The wave frequency used is $\omega(L/g)^{1/2} = 2.0$, with a wave amplitude of $\zeta a = 50$ mm.

Figure 19 shows a comparison of the time history curves for the ship's roll and heave motions under different loading conditions. It is observed that the maximum roll amplitude of 7.0° occurs in the no-load case. However, the roll amplitude decreases to 3.5° under the 20 % loading rate. As the loading rate increases from 57.5 % to 70 %, the roll amplitude gradually decreases, although it remains higher than the roll amplitude at the 20 % loading rate. In contrast, the heave amplitude of the simplified LNG vessel in beam waves shows only slight variation across different loading rates, with a small increase in heave amplitude as the tank loading rate increases.

To summarize, the results demonstrate that the tank loading rate considerably affects the roll motion of the LNG ship in beam waves. Figure 20 shows the movement of the ship at a 20 % filling rate in beam waves over one period in Case 14. Figure 21 shows the cross-section of the LNG ship, including both the internal and external fluid fields, at different loading rates in beam waves, with the largest roll angle occurring at $t = 5.1$ s.

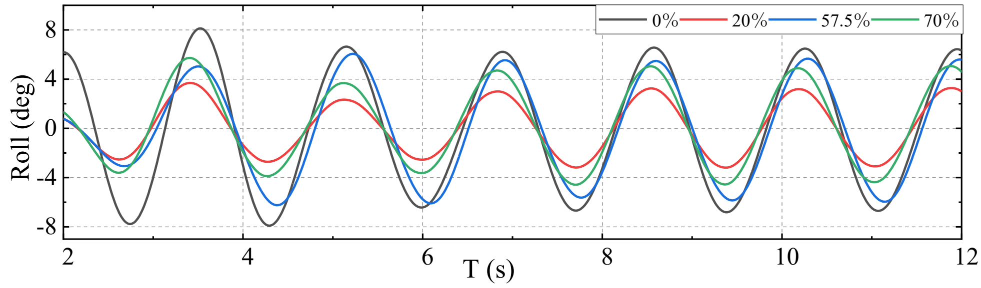

(a) Roll

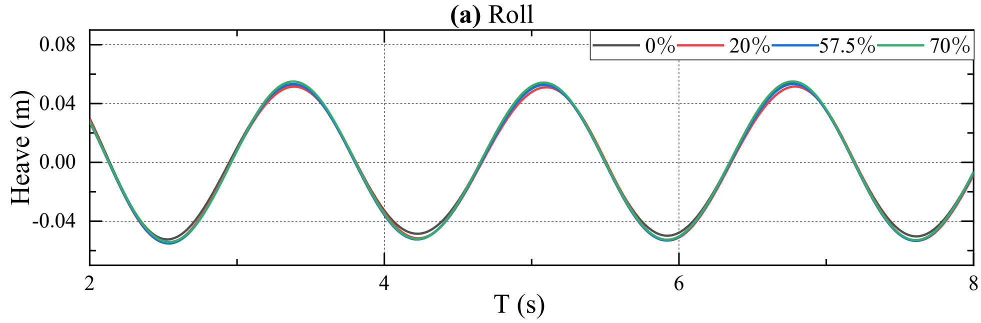

(b) Heave

Fig. 19 Time history curve of ship motions at different loading rates under beam waves (Cases 13–16)

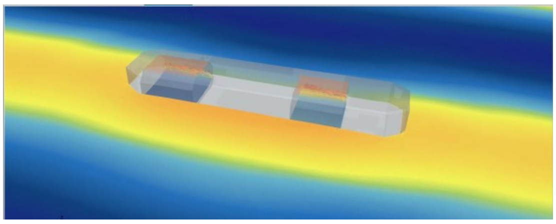

(a) t = T0

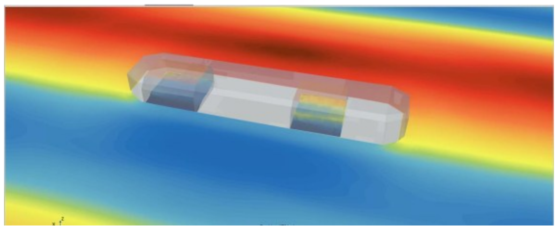

(b) t = T0 + 1/4T

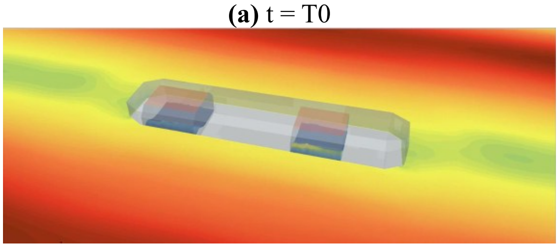

(c) t = T0 + 2/4T

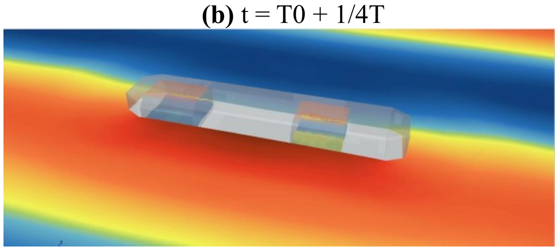

(d) t = T0 + 3/4T

Fig. 20 Motion procedure of the ship at 20 % filling rate in beam waves (Case 14)

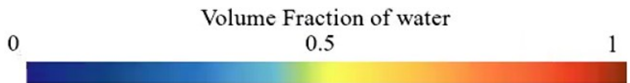

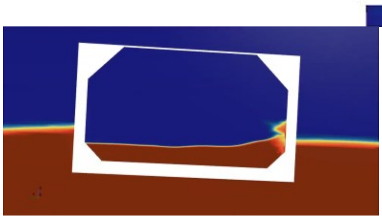

(a) Filling rate 20 % (Case 14)

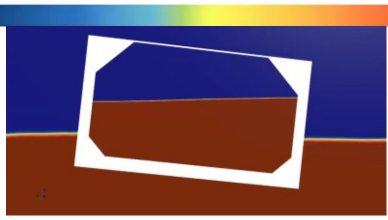

(b) Filling rate 57.5 % (Case 15)

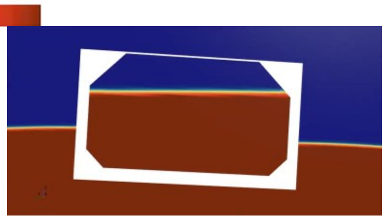

(c) Filling rate 70 % (Case 16)

Fig. 21 Comparison of inner and external fluid fields of the ship at different loading rates of 20 %, 57.5 %, and 70 % in beam waves (Cases 14–16)

5.5 Influence of forward speed on ship motions under head waves

In this section, simulations are performed for the ship at a 20 % tank filling rate with different forward speeds (*Fr* = 0.1, 0.2, and 0.3) sailing in the same wave conditions as Case 2. The impact of forward speed on the ship's responses and tank sloshing is analyzed. Figure 22 shows the grid refinement region around the ship for the forward speed cases, ensuring accurate capture of the ship-generated Kelvin waves in the wake area. A comparison of wave patterns and ship-generated waves at different speeds is shown in Figure 23. It is observed that for the lower speed case ($Fr = 0.1$), the ship-generated transverse waves are very short, and the Kelvin wave area is small. The ship-generated waves become more pronounced for ships with higher forward speeds.

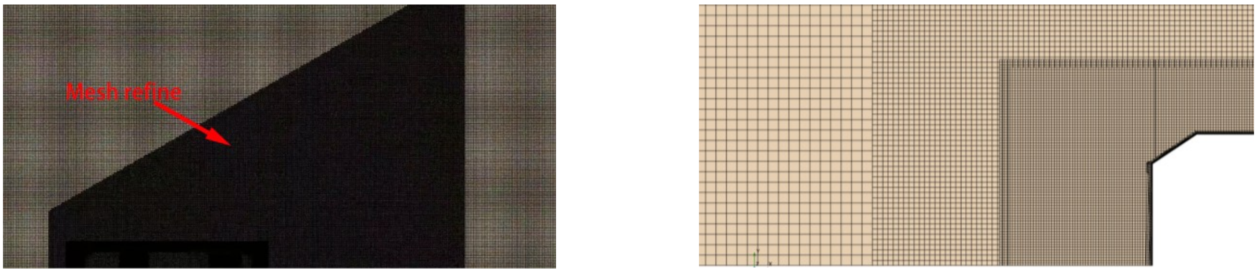

(a) Mesh refinement at the free surface **(b)** Mesh transition between fine and coarse grids

Fig. 22 Mesh refinement for cases with forward speed

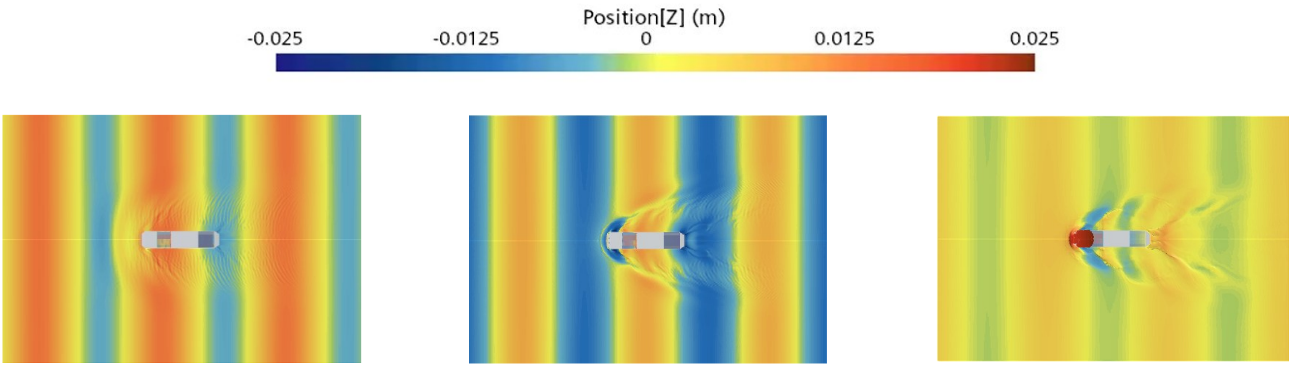

(a) $Fr = 0.1$ (Case 17) **(b)** $Fr = 0.2$ (Case 18) **(c)** $Fr = 0.3$ (Case 19)

Fig. 23 Wave pattern around the ship at different speeds (Cases 17–19)

Figure 24 compares the local views of the internal and external flow fields of the ship at different forward speeds, at the same solution time instant. As the Froude number increases from $Fr = 0$–0.2, the sloshing in the internal tanks becomes more pronounced. However, when the speed reaches $Fr = 0.3$, the internal tank sloshing becomes less intense.

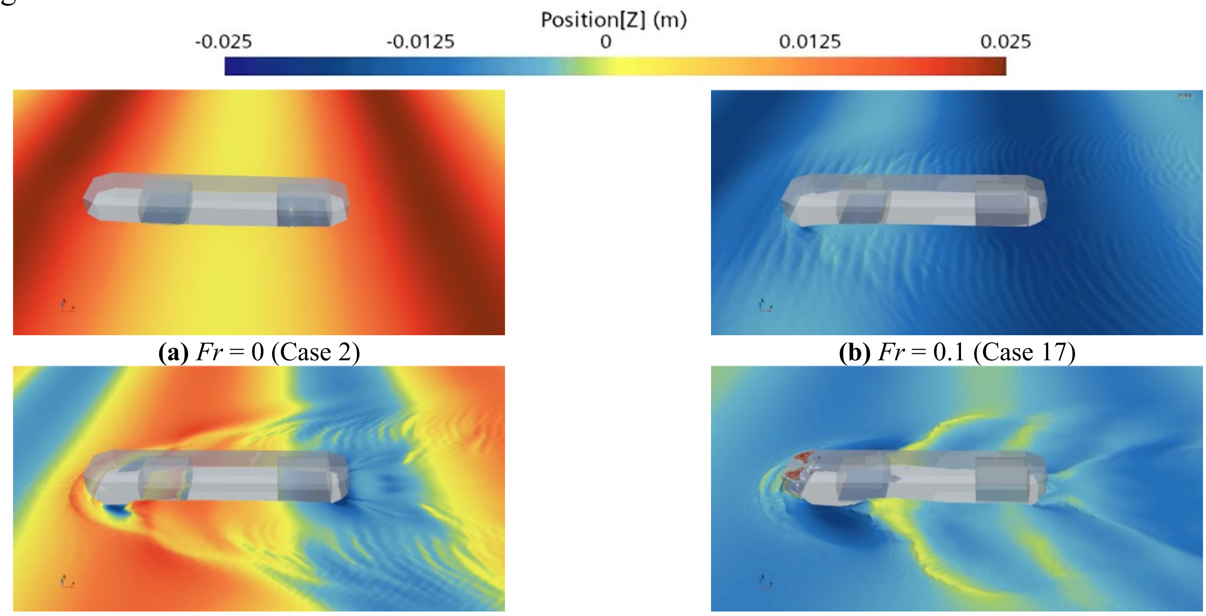

(a) $Fr = 0$ (Case 2) **(b)** $Fr = 0.1$ (Case 17)

(c) $Fr = 0.2$ (Case 18) **(d)** $Fr = 0.3$ (Case 19)

Fig. 24 Internal and external flow fields of the ship with different forward speeds at the same solution time instant (Cases 2 and 17–19)

Figure 25 compares the time series of heave and pitch motions at different speeds. The heave amplitude shows an increasing trend as the ship speed increases from Fr = 0–0.3, indicating a clear relationship between the ship's speed and heave motion, where higher speeds result in greater heave amplitude. The difference in pitch amplitude across different speed cases is minimal, although the pitch at zero speed is slightly smaller than in the other cases. Additionally, the wave encounter frequency increases as the ship speed increases.

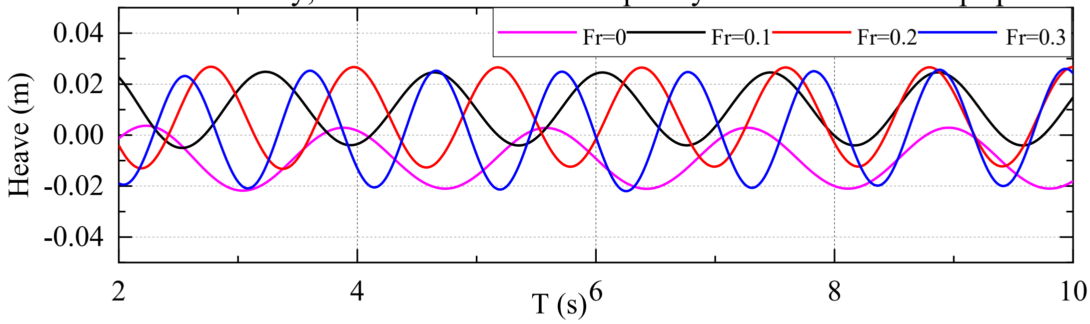

(a) Heave

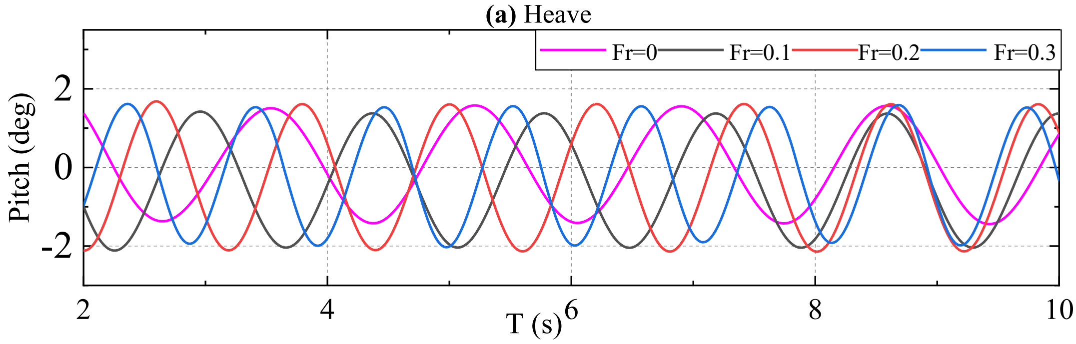

(b) Pitch

Fig. 25 Time history of ship longitudinal motions at different speeds (Cases 2 and 17–19)

6. Impact loads owing to tank sloshing

6.1 Pressure distribution on the tank's inner surface

Accurate prediction of the oscillatory fluid load on the tank's bulkhead is essential for analyzing sloshing load responses and evaluating structural strength. Cases 7 (beam wave) and 8 (head wave) are selected to investigate the impact loads caused by tank sloshing on the bulkhead. Both cases have the same wave frequency ($\omega(L/g)^{1/2} = 3.25$), wave amplitude (ζ_a = 50 mm), and tank loading rate (20 %). The locations of the pressure monitoring points in the tank are shown in Figure 26. Two monitoring points, Q1 and Q2, are chosen to assess the pressure distribution on the surface of the forward liquid tank of the simplified LNG vessel under beam waves. Four measuring points, P1, P2, P3, and P4, are selected to monitor the pressure on the forward surface of the fore tank under head waves.

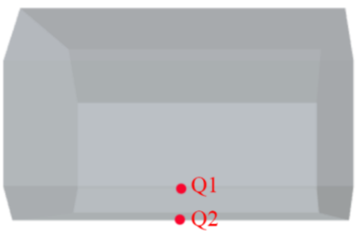

(a) Side view

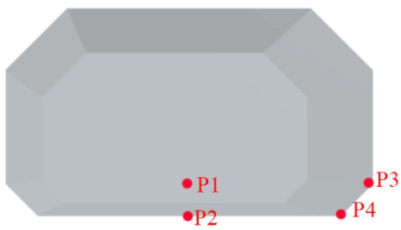

(b) Front view

Fig. 26 Position of pressure monitor points on the fore tank's inner surface

The time history of the slamming pressure at these locations for the ship in beam and head waves is shown in Figure 27. Figure 27(a) shows that under the beam wave, the pressure exhibits a pronounced multi-peak phenomenon, which is attributed to the intense tank sloshing caused by the ship's substantial roll motion. Nonlinear phenomena, such as the breakup of the free surface in the tank, are clearly observed. Point Q1 is situated at the boundary between wet and dry states. In contrast, under the head wave case in Figure 27(b), the free surface flow in the tank remains relatively stable owing to the low-amplitude pitch motion. As a result, the pressure distribution in the tank follows a more linear pattern. The pressure is mainly caused by hydrostatic forces, with fluctuations arising from the mild sloshing flow.

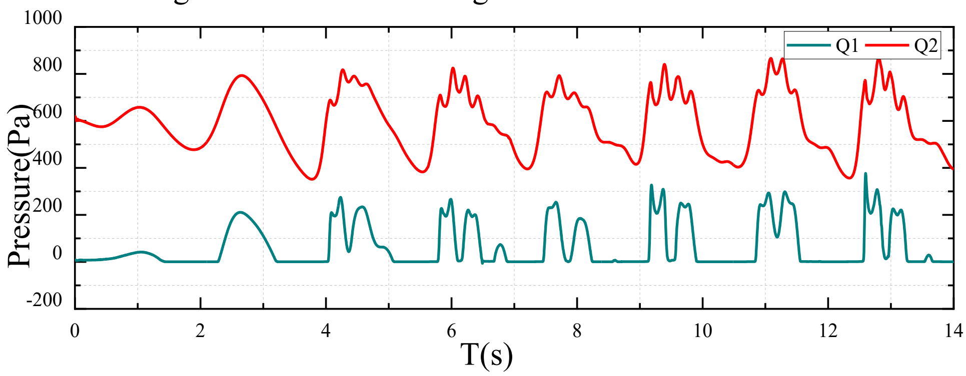

(a) Beam wave (Case 7)

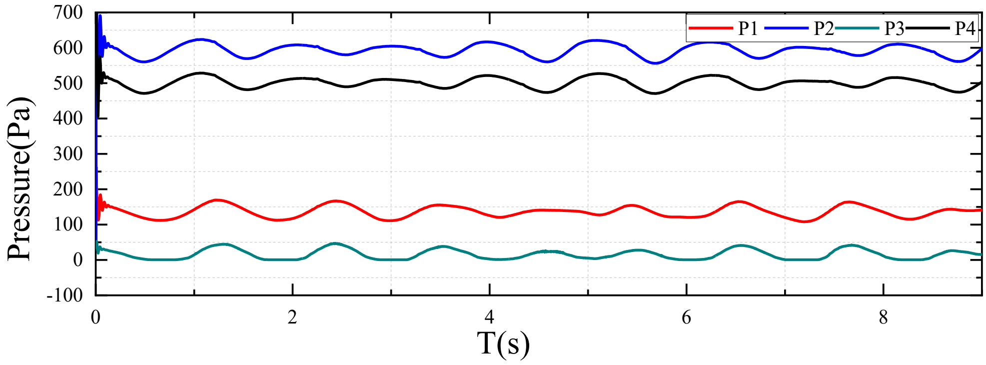

(b) Head wave (Case 8)

Fig. 27 Time history of tank sloshing pressure of the ship in beam and head waves

Figure 28 shows the sloshing behavior in the fore tank over one period under both beam and head waves. It is clear that sloshing is considerably more intense in the beam wave case, where phenomena such as solitary waves and wave breaking occur, compared to the head wave case, where the ship's longitudinal motion is relatively mild. This observation aligns with the time history curve data of the sloshing pressure.

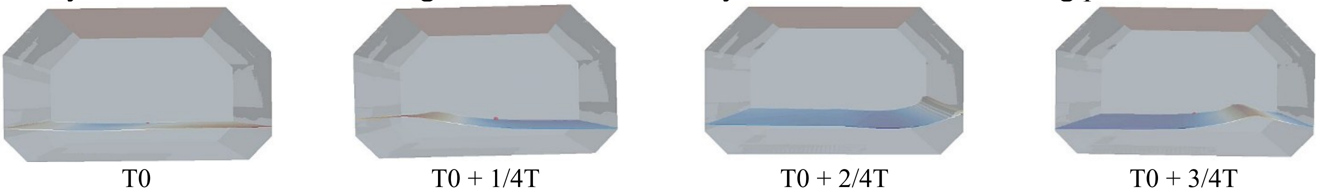

(a) Beam wave (Case 7)

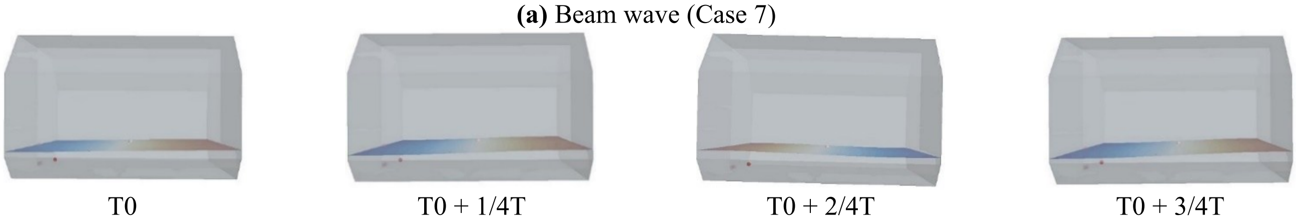

(b) Head wave (Case 8)

Fig. 28 Tank sloshing at typical time instants in beam and head waves

6.2 Influence of tank loading rate on sloshing loads under head waves

The sloshing pressure on the bulkhead for the ship at three different loading rates - 20 %, 57.5 %, and 70 % - under head wave conditions (Cases 10–12) is compared. The wave parameters, including wave frequency ($\omega(L/g)^{1/2} = 2$) and wave height ($\zeta a = 50$ mm), are kept constant. Figure 29 shows the time history curve of tank sloshing at points P3 and P4 for the three loading rate cases. It can be observed that the sloshing frequency remains nearly identical across all loading rates, indicating that the ship's motion frequency in head waves for all three cases corresponds to the wave encounter period. The time history curves of the pressure show steady wave fluctuations for the 57.5 % and 70 % loading rate cases. Although the pressure increases with the tank filling rate, the sloshing effect and free surface motion become milder. In contrast, for the 20 % loading rate case, the sloshing pressure exhibits a pulsed behavior because point P3 is located at a position where the tank alternates between dry and wet states.

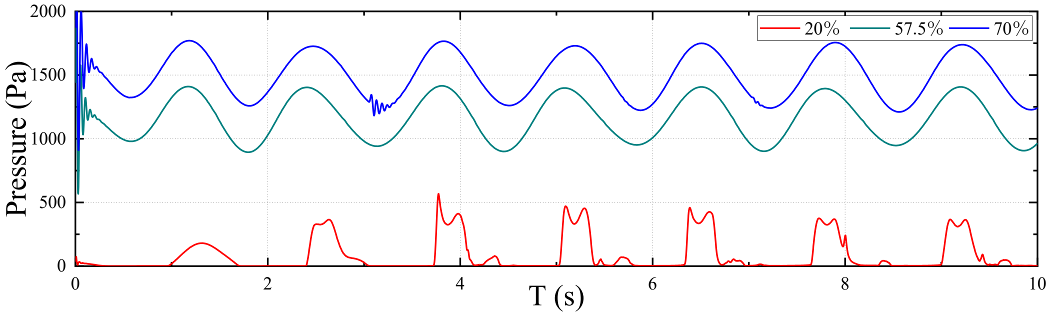

(a) Pressure at P3

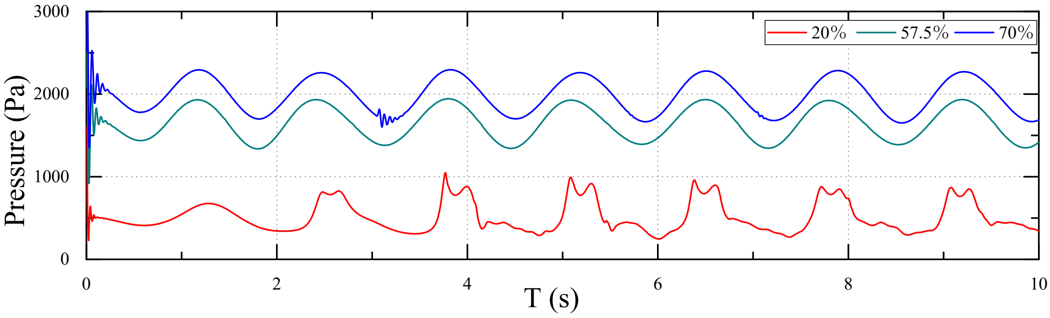

(b) Pressure at P4

Fig. 29 Time history curve of pressure on the tank bulkhead under head waves (Cases 10–12)

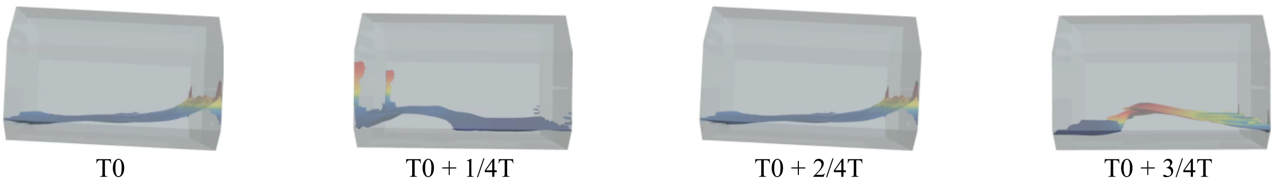

(a) 20 % filling rate (Case 10)

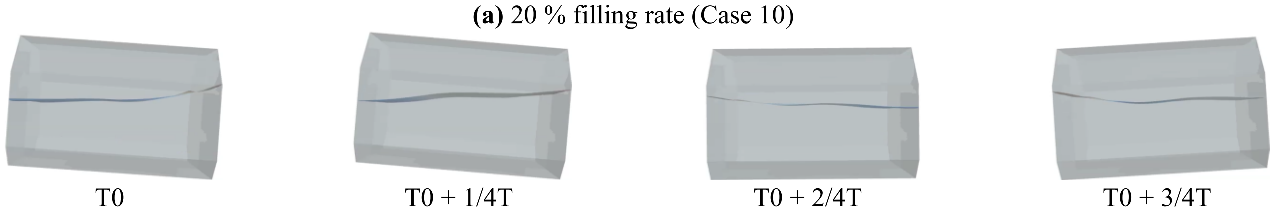

(b) 57.5 % filling rate (Case 11)

(c) 70 % filling rate (Case 12)

Fig. 30 Tank sloshing at different loading rates under head waves (Cases 10–12)

Figure 30 compares the sloshing fluid in the tank at typical time instants during one wave cycle for the three different loading rates. The sloshing phenomenon is more intense in the 20 % low loading rate case, with noticeable free surface breakage and fluid splash, which aligns with the pressure time series data. In contrast, the free surface remains relatively calm in the case of a 70 % high loading rate. The severity of tank sloshing is influenced by the relationship between the ship's motion period and the natural period of tank sloshing at varying filling rates. As shown in Table 3, the 1st-order natural frequencies of tank sloshing for loading rates of 20 %, 57.5 %, and 70 % are $\omega_1(L/g)^{1/2}$ = 2.782, 4.013, and 4.157, respectively. The incident wave frequency is $\omega(L/g)^{1/2} = 2$. Therefore, the most severe tank sloshing occurs at the 20 % loading rate because its frequency is closest to the 1st-order natural frequency of the tank sloshing.

6.3 Influence of tank loading rate on sloshing loads under beam waves

The sloshing-induced pressure on the side bulkhead of the LNG carrier under beam wave conditions is analyzed for three different tank filling rates of 20 %, 57.5 %, and 70 % (Cases 14–16). The same wave conditions, with a wave frequency of $\omega(L/g)^{1/2} = 2$ and a wave height of $\zeta a = 50$ mm, are used for all three cases. Figure 31 shows the time history curves of tank sloshing at the pressure monitoring points Q1 and Q2 for the three loading rates. It is observed that the sloshing frequency remains consistent across the three cases and matches the roll frequency of the ship. At the Q1 pressure monitoring point with a 20 % low filling rate, a clear multimodal phenomenon is observed. The pressure exerted by liquid sloshing on the bulkhead increases as the tank filling rate increases, and the curve trends become smoother. Compared to head wave conditions, liquid sloshing in the tank is more severe under beam waves. The maximum impact pressure at a 70 % tank filling rate reaches nearly 3,000 Pa, considerably higher than the 2,300 Pa measured under head wave conditions. This highlights the increased sloshing impact risk posed by beam waves at high filling levels.

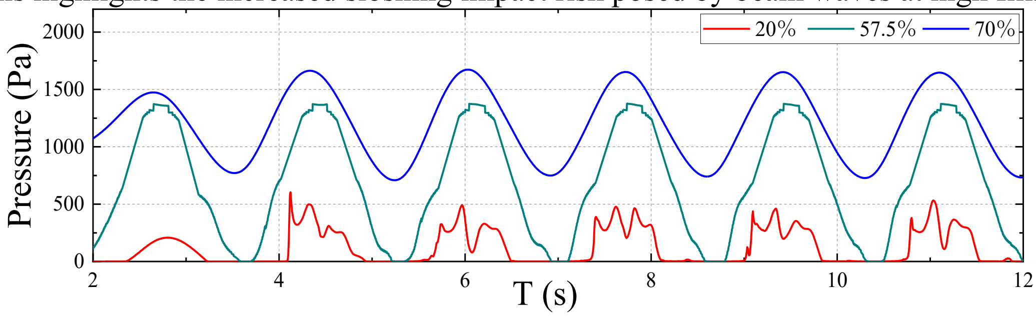

(a) Pressure at Q1

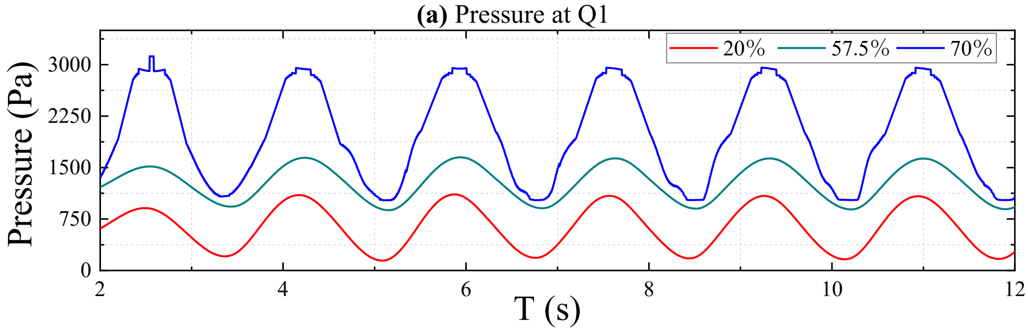

(b) Pressure at Q2

Fig. 31 Time history curve of pressure on the tank bulkhead under beam waves (Cases 14–16)

Figure 32 shows the internal flow field in the fore tank under beam waves during one wave period, comparing different filling rates. The free surface behavior in the tank shows three-dimensional effects when pitch, roll, and heave degrees-of-freedom are allowed under beam waves. Similar to the head wave cases, the tank sloshing effect is more pronounced at low filling rates, while the free surface tends to stabilize as the filling rate increases.

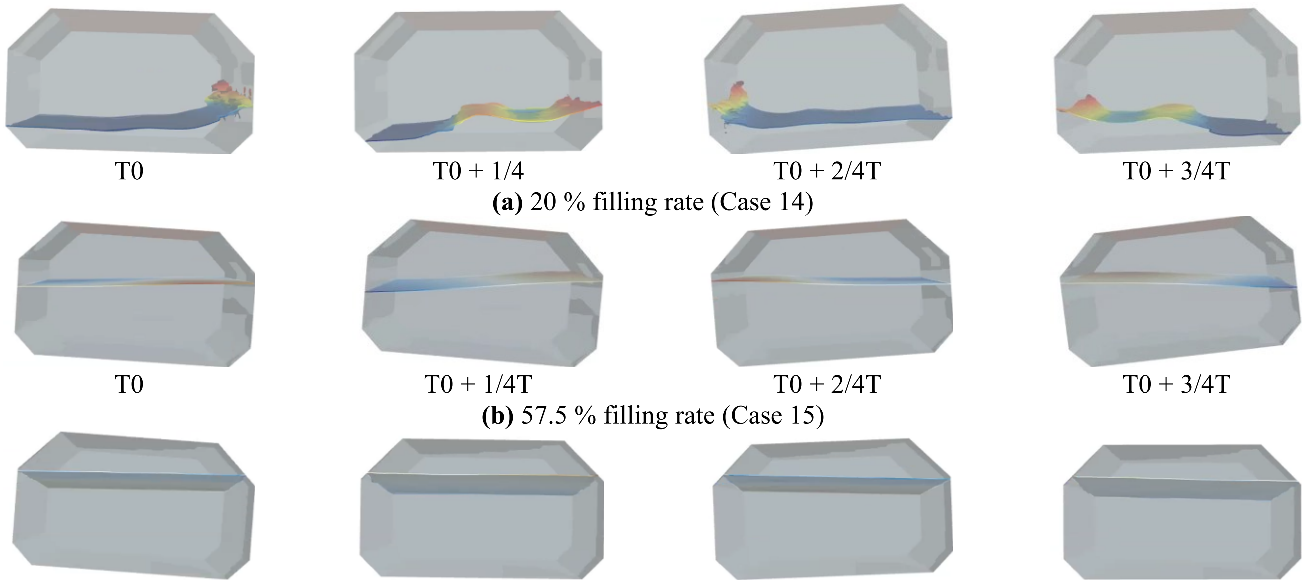

T0 T0 + 1/4 T0 + 2/4T T0 + 3/4T

(a) 20 % filling rate (Case 14)

T0 T0 + 1/4T T0 + 2/4T T0 + 3/4T

(b) 57.5 % filling rate (Case 15)

T0 T0 + 1/4T T0 + 2/4T T0 + 3/4T

(c) 70 % filling rate (Case 16)

Fig. 32 Tank sloshing at different loading rates under beam waves (Cases 14–16)

6.4 Influence of forward speed on tank sloshing under head waves

Figure 33 shows the time series of pressure at points P1–P4 for different ship forward speeds of $Fr = 0$, 0.1, 0.2, and 0.3. The peak pressure values at these positions for different ship speeds are summarized in Table 7. It is clear that the sloshing pressure peak on the bulkhead increases as the Froude number increases from $Fr = 0$–0.2. However, when the Froude number reaches $Fr = 0.3$, the slamming pressure on the bulkhead decreases. This behavior can be explained by the relationship between the natural resonance frequency of the liquid sloshing at a given height and the encounter frequency of the ship's motion through the waves. The wave encounter frequency of the ship can be calculated by:

$$\omega_e = \omega\left(1 - \frac{V\omega\cos\beta}{g}\right) \tag{11}$$

where V is the ship speed, ω is the wave natural frequency, and β is the heading angle. In these cases, by substituting $Fr = 0$, 0.1, 0.2, and 0.3 along with $\omega(L/g)^{1/2} = 2.0$, the resulting dimensionless wave encounter frequencies are $\omega_e(L/g)^{1/2} = 2.0$, 2.4, 2.8, and 3.2, respectively.

At a moderate speed of $Fr = 0.2$, the hull's wave encounter frequency ($\omega_e(L/g)^{1/2} = 2.8$) closely matches the natural frequency of the tank sloshing ($\omega_1(L/g)^{1/2} = 2.782$), resulting in considerable resonance effects in the liquid. At lower or higher speeds, specifically when the Froude number is $Fr = 0$ or 0.3, the hull's motion frequency deviates from the natural sloshing frequency, which decreases the sloshing intensity and leads to comparatively lower slamming pressure. The sloshing behavior, including fore tank motions and free surface patterns over one wave period at different ship speeds, is shown in Figure 34, providing a clearer understanding of the sloshing pressure under various conditions.

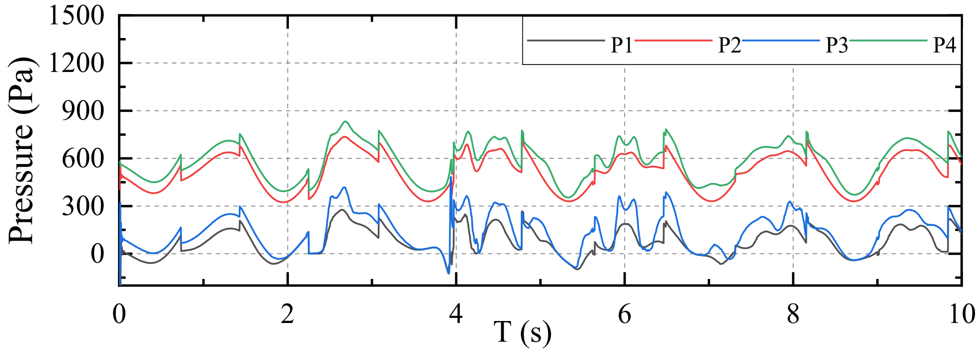

(a) *Fr* = 0 (Case 2)

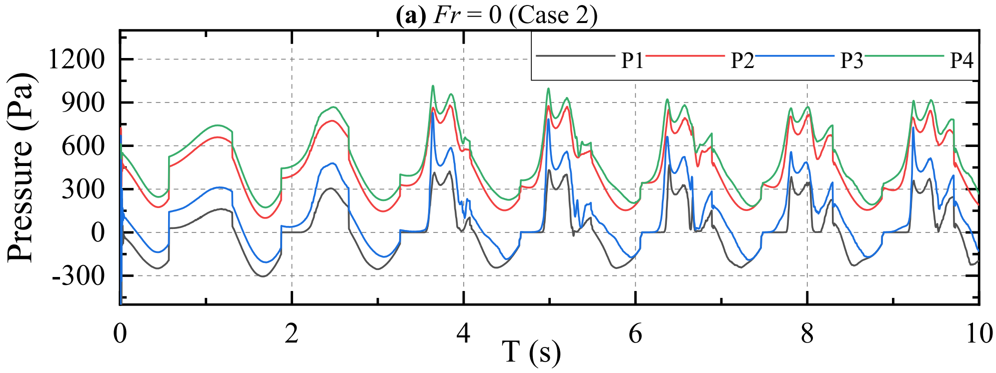

(b) *Fr* = 0.1 (Case 17)

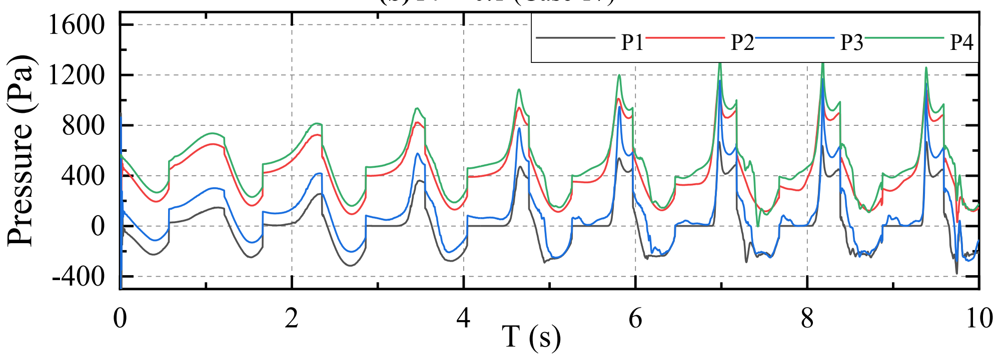

(c) *Fr* = 0.2 (Case 18)

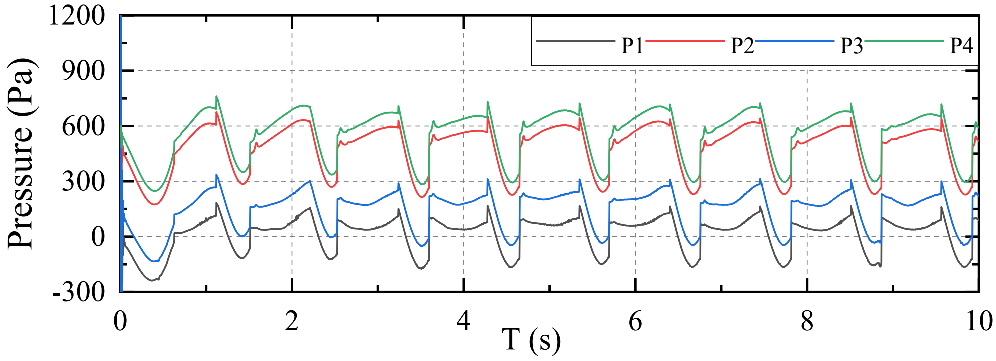

(d) *Fr* = 0.3 (Case 19)

Fig. 33 Time history curve of tank sloshing pressure in head waves at different ship speeds (Case 2 and Cases 17–19)

Table 7 Pressure peaks at the monitoring points at different ship speeds

Case	*Fr*	P1 (Pa)	P2 (Pa)	P3 (Pa)	P4 (Pa)
2	0	224	682	467	758
17	0.1	461	842	784	1,013
18	0.2	614	1,002	1,144	1,211
19	0.3	148	631	296	723

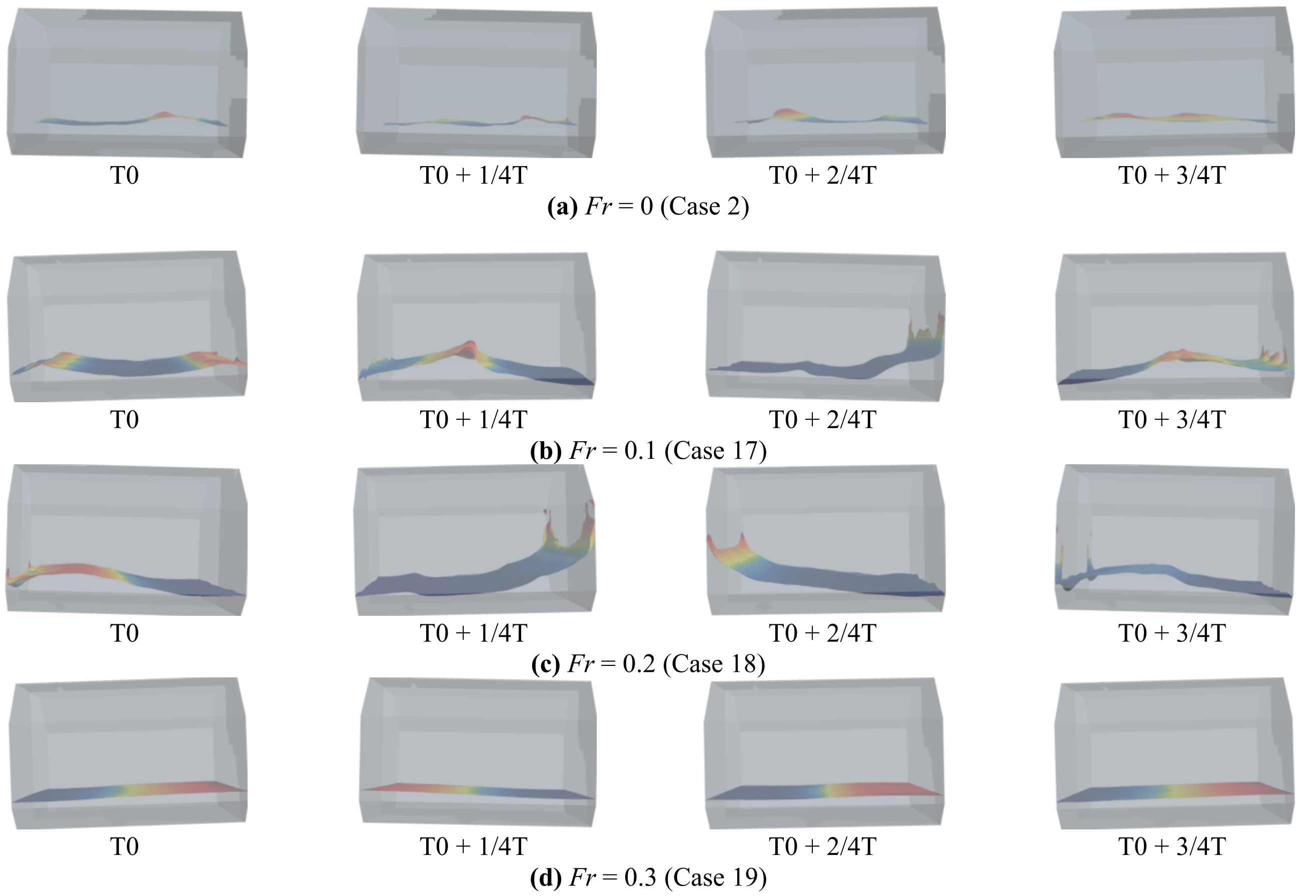

Fig. 34 Tank sloshing at typical time instants under head waves at different ship speeds (Case 2 and Cases 17–19)

7. Conclusions

In this study, simulations of the LNG ship seakeeping problem were performed using the CFD-based STAR-CCM+ tool, employing overset grid technology and the VOF method. The motion response of the LNG ship was analyzed under the coupled interaction of internal and external flow fields in regular waves, both with and without ship speed. The following conclusions can be made.

(1) The current RANS method effectively simulates the independent tank sloshing phenomenon, showing good agreement with results from MPS and experiments. While the RANS simulation accurately captures the overall trend of impact pressure and aligns well with experimental observations, it has limitations in accurately representing the liquid splash phenomenon.

(2) The tank filling rate considerably influences the roll-free decay period, indicating that tank sloshing affects the ship's natural roll frequency. This influence is more pronounced on ship roll motion in beam waves compared to other degrees-of-freedom or in head waves.

(3) As the Froude number increases from Fr = 0–0.2, the sloshing in the internal tanks becomes increasingly intense. However, when the speed reaches Fr = 0.3, the internal tank sloshing subsides. This behavior is attributed to the relationship between the natural resonance frequency of the liquid sloshing at a specific height and the ship's encounter frequency.

ACKNOWLEDGEMENTS

This research is supported by the National Natural Science Foundation of China (No. 52271316) and the Science and Technology Project in Guangzhou (No. 2024A04J9886).

REFERENCES

[1] Tuswan, T., Sari, D. P., Muttaqie, T., Prabowo, A. R., Soetardjo, M., Murwantono, T. T. P., Utina, R., Yuniati, Y., 2023. Representative application of LNG-fuelled ships: a critical overview on potential GHG emission reductions and economic benefits. *Brodogradnja*, 74(1), 63-83. https://doi.org/10.21278/brod74104

[2] Huang, S., Duan, W. Y., Ma, Q. W., Zhu, X., Wu, H. T., 2013. Research progress on sloshing and coupling motion of sloshing and ship. *Journal of Ship Mechanics*, 17(10), 1209-1220.

[3] Pistani, F., Thiagarajan, K., 2012. Experimental measurements and data analysis of the impact pressures in a sloshing experiment. *Ocean engineering*, 52, 60-74. https://doi.org/10.1016/j.oceaneng.2012.06.002

[4] Godderidge, B., Turnock, S. R., Tan, M., 2012. Evaluation of a rapid method for the simulation of sloshing in rectangular and octagonal containers at intermediate filling levels. *Computers & Fluids*, 57, 1-24. https://doi.org/10.1016/j.compfluid.2011.09.010

[5] Antuono, M., Lugni, C., 2018. Global force and moment in rectangular tanks through a modal method for wave sloshing. *Journal of Fluids and Structures*, 77, 1-18. https://doi.org/10.1016/j.jfluidstructs.2017.11.004

[6] Kaminski, M. L., Bogaert, H., 2009. Full scale sloshing impact tests. *Proceedings of the Nineteenth International Offshore and Polar Engineering Conference*, June 21-26, 2009, Osaka, Japan.

[7] Journee, J. M. J., 1997. Liquid Cargo and Its Effect on Ship Motions. *Proceedings of the 6th International Conference on Stability of Ships and Ocean Vehicles*, September 22-27, 1997, Varna, Bulgaria.

[8] Molin, B., 2002. LNG-FPSO's: frequency domain, coupled analysis of support and liquid cargo motion. *Proceedings of the IMAM conference,* Rethymnon, Greece.

[9] Newman, J. N., 2005. Wave effects on vessels with internal tanks. *Proceedings of the 20th Workshop on Water Waves and Floating Bodies*, May 29 – June 1, Spitsbergen, Norway.

[10] Kim, Y., Nam, B. W., Kim, D. W., Kim, Y. S., 2007. Study on coupling effects of ship motion and sloshing. *Ocean Engineering*, 34(16), 2176-2187. https://doi.org/10.1016/j.oceaneng.2007.03.008

[11] Tabri, K., Matusiak, J., Varsta, P., 2009. Sloshing interaction in ship collisions - An experimental and numerical study. *Ocean Engineering*, 36(17-18), 1366-1376. https://doi.org/10.1016/j.oceaneng.2009.08.017

[12] Li, H., Sun, Z., Han, B., Shao, Y., Deng, B., 2022. Research on the motion response of aquaculture ship and tank sloshing under rolling resonance. *Brodogradnja*, 73(2), 1-15. https://doi.org/10.21278/brod73201

[13] Martić, I., Degiuli, N., Ćatipović, I., 2016. Evaluation of the added resistance and ship motions coupled with sloshing using potential flow theory. *Brodogradnja*, 67(4), 109-122. https://doi.org/10.21278/brod67408

[14] Mikulec, M., Piehl, H., 2023. Verification and validation of CFD simulations with full-scale ship speed/power trial data. *Brodogradnja*, 74(1), 41-62. https://doi.org/10.21278/brod74103

[15] Yue, B., Tang, Y., 2016. Numerical simulation of three dimensional large amplitude liquid sloshing in spherical containers. *Journal of Astronautics*, 37(12), 1405-1410.

[16] Kim, M., Turan, O., Day, S., Incecik, A., 2018. Numerical studies on added resistance and ship motions of KVLCC2 in waves. *Trends and Challenges in Maritime Energy Management*, 6, 111-126. https://doi.org/10.1007/978-3-319-74576-3_9

[17] Yin, C., Zhuang, Y., Wan, D., 2016. Numerical study on liquid sloshing in LNG tanks coupled with ship motion in waves. *Proceedings of 3rd International Conference on Violent Flows*, March 9-11, 2016, Osaka, Japan.

[18] Zhuang, Y., Wan, D., 2019. Numerical study on ship motion fully coupled with LNG tank sloshing in CFD method. *International Journal of Computational Methods*, 16(06), 1840022. https://doi.org/10.1142/S0219876218400224

[19] Jiao, J., Zhao, M., Jia, G., Ding, S., 2024. SPH simulation of two side-by-side LNG ships' motions coupled with tank sloshing in regular waves. *Ocean Engineering*, 297, 117022. https://doi.org/10.1016/j.oceaneng.2024.117022

[20] Wang, Z. H., Jiang, S. C., Geng, B. L., 2024. Coupling analysis of liquid sloshing and box sway motion under irregular wave actions. *Ocean Engineering*, 291, 116451. https://doi.org/10.1016/j.oceaneng.2023.116451

[21] Liu, L., Feng, D., Wang, X., Zhang, Z., Yu, J., Chen, M., 2022. Numerical study on the effect of sloshing on ship parametric roll. *Ocean Engineering*, 247, 110612. https://doi.org/10.1016/j.oceaneng.2022.110612

[22] Ma, C., Oka, M., 2019. Numerical coupling model based on SPH and panel method to solve the sloshing effect on ship motion in wave condition. *Proceedings of the Twenty-ninth International Ocean and Polar Engineering Conference*, June 16-21, 2019, Honolulu, Hawaii, USA.

[23] Ding, S., Jiao, J.L., Zhao, M.M., 2023. Influence of 2D and 3D SPH simulation on tank sloshing coupled with floating body motions. *Shipbuilding of China,* 64(1), 180–191.

[24] Cheng, C., 2020. Parallel Numerical Simulation of Liquid Sloshing and Multiphase Flow Problems Based on SPH Method. *Master Thesis*, Dalian University of Technology, Dalian, China.

[25] Pilloton, C., Bardazzi, A., Colagrossi, A., Marrone, S., 2022. SPH method for long-time simulations of sloshing flows in LNG tanks. *European Journal of Mechanics-B/Fluids*, 93, 65-92. https://doi.org/10.1016/j.euromechflu.2022.01.002

[26] Trimulyono, A., Atthariq, H., Chrismianto, D., Samuel, S., 2022. Investigation of sloshing in the prismatic tank with vertical and T-shape baffles. *Brodogradnja*, 73(2), 43-58. https://doi.org/10.21278/brod73203

[27] Versteeg, H. K., & Malalasekera, W., 2007. An Introduction to Computational Fluid Dynamics: The Finite Volume Method, *Pearson Education*.

[28] Weller, H. G., Tabor, G., Jasak, H., Fureby, C., 1998. A tensorial approach to computational continuum mechanics using object-oriented techniques. *Computers in Physics*, 12(6), 620–631. https://doi.org/10.1063/1.168744

[29] Siemens PLM Software, 2021. STAR-CCM+ User Guide, Version 2021.1. Siemens Digital Industries Software.

[30] Menter, F. R., 1994. Two-equation eddy-viscosity turbulence models for engineering applications. *AIAA Journal*, 32(8), 1598–1605. https://doi.org/10.2514/3.12149

[31] Kang, D. H., Lee, Y. B., 2005. Summary report of sloshing model test for rectangular model. *Daewoo Shipbuilding & Marine Engineering Co., Ltd.* South Korea.

[32] Xie, F. Z., Zhao, W. W., Wan, D. C., 2020. CFD simulations of three-dimensional violent sloshing flows in tanks based on MPS and GPU. *Journal of Hydrodynamics*, 32(4), 672-683. https://doi.org/10.1007/s42241-020-0039-8

[33] Gou, Y., Kim, Y., Kim, T. Y., 2011. A numerical study on coupling between ship motions and sloshing in frequency and time domains. *Proceedings of the Twenty-first International Offshore and Polar Engineering Conference,* June 19-24, 2011, Maui, Hawaii, USA.

[34] Nam, B. W., Kim, Y., Kim, D. W., Kim, Y. S., 2009. Experimental and numerical studies on ship motion responses coupled with sloshing in waves. *Journal of Ship Research*, 53(02), 68-82. https://doi.org/10.5957/jsr.2009.53.2.68